

# Interferometric imaging of carbon monoxide in comet C/1995 O1 (Hale-Bopp): evidence for a strong rotating jet

D. Bockelée-Morvan<sup>1</sup>, F. Henry<sup>1</sup>, N. Biver<sup>1</sup>, J. Boissier<sup>2</sup>, P. Colom<sup>1</sup>, J. Crovisier<sup>1</sup>, D. Despois<sup>3</sup>, R. Moreno<sup>1</sup>, and J. Wink<sup>2\*</sup>

<sup>1</sup> Observatoire de Paris, F-92195 Meudon, France

<sup>2</sup> IRAM, 300 rue de la Piscine, Domaine universitaire, F-38406, Saint Martin d'Hères, France

<sup>3</sup> Observatoire de Bordeaux, BP 89, F-33270 Floirac, France

October 19, 2021

## ABSTRACT

**Context.** Observations of the CO  $J(1-0)$  115 GHz and  $J(2-1)$  230 GHz lines in comet C/1995 O1 (Hale-Bopp) were performed with the IRAM Plateau de Bure interferometer on 11 March, 1997. The observations were conducted in both single-dish (ON-OFF) and interferometric modes with  $0.13 \text{ km s}^{-1}$  spectral resolution. Images of CO emission with  $1.7$  to  $3''$  angular resolution were obtained.

**Aims.** The ON-OFF and interferometric spectra show a velocity shift with sinusoidal time variations related to the Hale-Bopp nucleus rotation of 11.35 h. The peak position of the CO images moves perpendicularly to the spin axis direction in the plane of the sky. This suggests the presence of a CO jet, which is active night and day at about the same extent, and is spiralling with nucleus rotation. The high quality of the data allows us to constrain the characteristics of this CO jet.

**Methods.** We have developed a 3-D model to interpret the temporal evolution of CO spectra and maps. The CO coma is represented as the combination of an isotropic distribution and a spiralling gas jet, both of nucleus origin.

**Results.** Spectra and visibilities (the direct output of interferometric data) analysis shows that the CO jet comprises  $\sim 40\%$  the total CO production and is located at a latitude  $\sim 20^\circ$  North on the nucleus surface. Our inability to reproduce all observational characteristics shows that the real structure of the CO coma is more complex than assumed, especially in the first thousand kilometres from the nucleus. The presence of another moving CO structure, faint but compact and possibly created by an outburst, is identified.

**Key words.** Comets: individual: C/1995 O1 (Hale-Bopp) – Radio lines: solar system – Techniques: interferometric

## 1. Introduction

Millimetre spectroscopy provided many insights into the composition and physical properties of cometary atmospheres. Many cometary parent molecules issued from the nucleus were identified with this technique. The high spectral resolution capabilities, and the possibility to observe several rotational lines belonging to the same molecule, allowed us to retrieve unique information concerning the velocity and temperature of the expanding coma, and the anisotropy of gas production at the nucleus surface. Because of the low, diffraction-limited spatial resolution provided by radio dishes at millimetric wavelengths, at best typically  $10''$ , studies concerning the spatial distribution of parent molecules in the coma were sparse.

The exceptional brightness of comet C/1995 O1 (Hale-Bopp) near its perihelion on 1 April, 1997, motivated a wealth of innovative cometary observations. Among them, interferometric imaging of rotational transitions of parent molecules was successfully attempted. The Berkeley-Illinois-Maryland Association (BIMA) array mapped comet Hale-Bopp in HCN  $J(1-0)$  and CS  $J(2-1)$  with  $9''$  angu-

lar resolution. Spatial asymmetries suggesting the presence of gas jets were detected (Veal et al., 2000; Wright et al., 1998; Woodney et al., 2002). Constraints on the photodissociative scalelengths of HCN and CS were obtained from the radial extent of their radio emissions (Snyder et al., 2001). Using the Owens Valley Radio Observatory (OVRO) millimetre array, Blake et al. (1999) obtained maps of HCN, DCN, HNC and HDO at  $2-4''$  spatial resolutions over  $2-3$  h integration time. The presence of arc-like structures offset from the nucleus is reported for all species but HCN, and interpreted in terms of jets of icy particles releasing unaltered gas contrasting with that outgassed from the nucleus.

Interferometric observations of rotational lines in comet Hale-Bopp were also made with the Plateau de Bure interferometer (PdBI) of the Institut de Radio Astronomie Millimétrique (IRAM) at  $1-3''$  resolution. A short and preliminary account of these observations was given in Wink et al. (1999), Despois (1999) and Henry et al. (2002). Millimetre lines of CO, HCN, CS, HNC,  $\text{CH}_3\text{OH}$ ,  $\text{H}_2\text{S}$ , SO,  $\text{H}_2\text{CO}$  were mapped (Wink et al., 1999; Boissier et al., 2007). At the same time, continuum maps of the dust and nucleus thermal emissions were obtained (Altenhoff et al., 1999). The PdBI was also used in single-dish mode to

Send offprint requests to: D. Bockelée-Morvan, e-mail: dominique.bockelee@obspm.fr

\* deceased

detect new cometary molecules (Bockelée-Morvan et al., 2000; Crovisier et al., 2004a,b).

We present here observations of the CO  $J(1-0)$  (115 GHz) and  $J(2-1)$  (230 GHz) lines performed on 11 March, 1997 at the Plateau de Bure interferometer. Among the  $\sim 20$  molecules identified in comet Hale-Bopp, and more generally in cometary atmospheres, carbon monoxide CO is of particular interest:

1. This species is the main agent of distant cometary activity, as first evidenced in comet 29P/Schwassmann-Wachmann 1 (Senay & Jewitt, 1994; Crovisier et al., 1995). This was later confirmed in comet Hale-Bopp from its long-term monitoring, which showed the change from a CO-dominated to an H<sub>2</sub>O-dominated activity at heliocentric distances  $r_h \sim 3-4$  AU (Biver et al., 1997, 1999a).
2. In comets within 3 AU from the Sun, CO is, most often, the second major gaseous component of the coma after water. CO production rates relative to water are highly variable from comet to comet, ranging from less than 1 % to  $\sim 20$  % (Irvine et al., 2000; Bockelée-Morvan et al., 2004, for a review). That measured in comet Hale-Bopp near perihelion is among the highest ever observed in comets:  $\sim 20$  % (e.g., Bockelée-Morvan et al., 2000; DiSanti et al., 2001).
3. There is much debate on CO production mechanisms. Because CO has a low sublimation temperature, the nucleus surface is certainly deprived of CO ice. Therefore, CO should outgas at some depth inside the nucleus, possibly from pure CO ice sublimation and/or from amorphous water ice when crystallizing and releasing trapped molecules (e.g., Enzian et al., 1998; Capria et al., 2000, 2002), if indeed pre-cometary ices condensed in amorphous form, which is somewhat debated (Mousis et al., 2000). Another mechanism proposed to explain the CO production of comet Hale-Bopp near perihelion is the release of CO trapped in crystalline water ice during water ice sublimation (Capria et al., 2000, 2002). Comparing the CO jets morphology, as the nucleus rotates, to those of less volatile species or dust might provide clues to the origin of CO.
4. There are several observational evidences that a significant part of the CO observed in cometary atmospheres could be produced by a distributed source. From in situ measurements of the local CO density in 1P/Halley with Giotto, Eberhardt et al. (1987) concluded that only about 1/3 of the CO originated from the nucleus. The spatial distribution of CO molecules deduced from infrared long-slit observations of comet Hale-Bopp led DiSanti et al. (1999, 2001) to suggest that one-half of the CO was released by a distributed source when comet Hale-Bopp was within 1.5 AU from the Sun. The spatial resolution of the CO maps obtained at PdBI, approximately 1000 km to 1700 km radius on the comet depending of the line observed, is below the estimated radial extension of the CO distributed source of  $\sim 5 \times 10^3$  km (DiSanti et al., 2001; Brooke et al., 2003). Therefore, an important aspect of the study of the CO PdBI interferometric data is that independent information concerning the existence of a CO distributed source in Hale-Bopp coma can be possibly obtained. The study of the radial distribution of the CO molecules is presented in

a separate paper (Bockelée-Morvan & Boissier, 2009). The brightness distribution of both 115 GHz and 230 GHz lines can be fully explained by pure nuclear CO production, provided that opacity effects and temperature variations in the coma are taken into account (Bockelée-Morvan et al., 2005; Bockelée-Morvan & Boissier, 2009).

The observations of the CO  $J(1-0)$  and  $J(2-1)$  lines, performed both in single-dish and interferometric modes, are presented in Sect. 2. They show evidence for a rotating CO jet. A model simulating a CO spiralling jet when the nucleus is rotating is developed in Sect. 3. It allowed us to compute synthetic spectra, visibilities and interferometric maps as a function of time, to be compared to the observations. Observations are analysed in Sect.4, and the model free parameters are retrieved. A discussion is given in Sect. 5.

## 2. Observations

### 2.1. Description

Comet C/1995 O1 (Hale-Bopp) was observed from 6 March to 22 March, 1997 with the Plateau de Bure interferometer of IRAM, located in the French Alps. The observations of the  $J(2-1)$  (230.538 GHz) and  $J(1-0)$  (115.271 GHz) CO rotational transitions were carried out on 11 March, from 4h to 15h UT. On this day, comet Hale-Bopp was at the geocentric distance  $\Delta = 1.368$  AU and heliocentric distance  $r_h = 0.989$  AU. The weather conditions were good to excellent and the atmospheric seeing was  $\sim 0.4''$  for both 1.3 and 3 mm receivers.

The comet was tracked using orbital elements provided by D.K. Yeomans (JPL, solution 55). The ephemeris was computed by P. Rocher (IMCCE, Observatoire de Paris) with a program which takes into account planetary perturbations. The first interferometric maps obtained on 9 March (HCN  $J(1-0)$  line) revealed that both continuum and molecular peak intensities were offset by about 5–6'' North in declination (Dec) from the nucleus position provided by the ephemeris. Observations on March 11 were made with the ephemeris corrected by 6'' North in Dec.

The PdBI was used in the compact configuration C1 (see Fig. 1) with five 15-m antennas providing 10 baselines (the spacing between two antennas) ranging from  $\sim 20$  to  $\sim 150$  m. In 1997, the PdBI comprised a flexible spectral correlator made of six independent units, providing correlated spectra with 64 to 256 channels spaced by 0.039 MHz to 2.5 MHz. We used 256 channels of 78 kHz separation for the observations of the 230 GHz line, and 256 channels of 39 kHz separation for those of the 115 GHz line. The four other units were used for the continuum observations presented in Altenhoff et al. (1999). The effective spectral resolution is a factor of 1.3 broader than the channel spacing, and corresponds to  $\sim 0.13$  km s<sup>-1</sup> for both lines.

The observing cycle was : pointing, focusing, 4 min of cross-correlation on the calibrators (2200+420 BL Lac, MWC349 and 3C373), 2 min of autocorrelation, and 51 one minute scans of cross-correlation on the comet interlaced with scans on the phase calibrator (2200+420 BL Lac) observed every 20 min. The cycle was completed by another 2 min of autocorrelation on Hale-Bopp. For the autocorrelation observations (in this mode, the five antennas

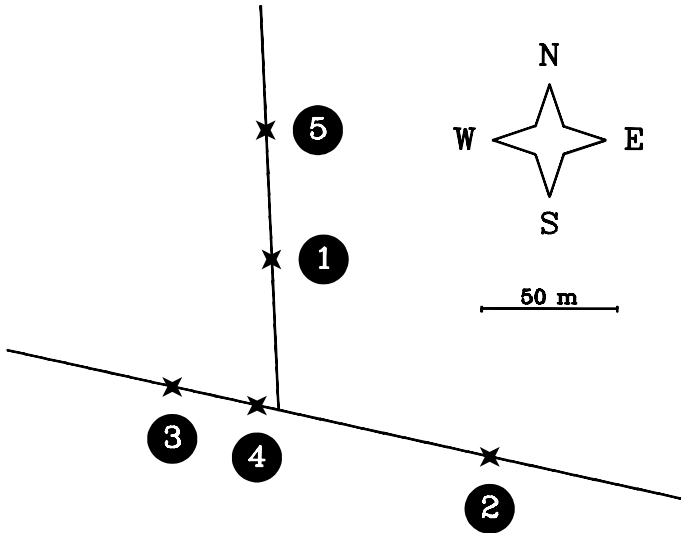


**Fig. 1.** The Plateau de Bure Interferometer in C1 configuration

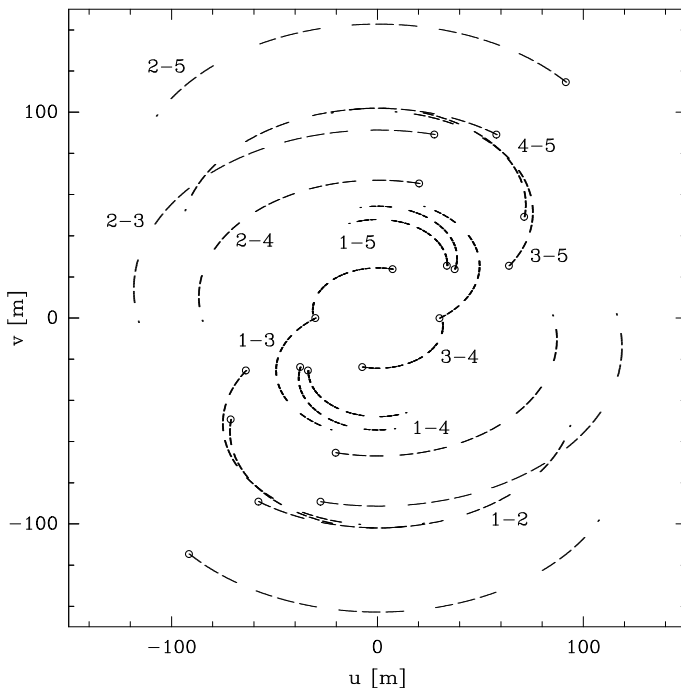


**Fig. 2.**  $uv$ -coverage at the PdBI on 11 March, 1997 with the C1 configuration. For each arc of ellipse, the white circle represents the  $uv$ -point at the beginning of the observations. The time evolution of the  $uv$ -points loci is counter-clockwise.

behave as five independent single-dish telescopes), we used position-switching (ON-OFF) with 5' offset to cancel the sky background. The spectra of the five antennas were then co-added. Hereafter, these autocorrelation observations will be denominated as ON-OFF observations.

The amplitude and phase calibrator was 2200+420. MWC349 was used to determine the flux density of 2200+420. Bandpass calibration was made on 3C273. Because of less accuracy in phase calibration after 12.5 h UT, only interferometric data acquired before 12.5 h UT were considered. Calibration was done with the IRAM

CLIC software, and the data hence derived were stored in  $uv$ -tables. Reduction and cleaning of the maps were performed with the MAPPING/GILDAS software<sup>1</sup>.

Concerning ON-OFF spectra, antenna temperatures  $T_A^*$  were converted into main beam brightness temperatures  $T_{mB}$  through  $T_{mB} = T_A^* F_{\text{eff}} / B_{\text{eff}}$  with beam efficiencies  $B_{\text{eff}}$  of 0.83 (115 GHz) and 0.58 (230 GHz), and forward efficiencies  $F_{\text{eff}}$  of 0.93 (115 GHz) and 0.89 (230 GHz). Flux density per beam ( $S$  in Jy) is then related to antenna temperature through  $S/T_A^* = (2k\Omega_{mB}/\lambda^2)F_{\text{eff}}/B_{\text{eff}} = 19.61F_{\text{eff}}/B_{\text{eff}}$ , where  $\Omega_{mB}$  is the main beam solid angle.

For both ON-OFF and interferometric data, the uncertainties in flux calibration are at most 10% and 15% for the  $J(1-0)$  and  $J(2-1)$  lines, respectively. The r.m.s in phase noise ranges from 10 to 27° at 230 GHz and from 4.6 to 20° at 115 GHz, depending of the baseline.

The cross-correlated spectra produce, for each spectral channel, interferometric maps with spatial resolutions corresponding to the  $uv$ -coverage (Fig. 2). When all cross-correlation data are considered, the full width at half maximum (FWHM) of the synthesized beam is  $2.00'' \times 1.38''$  with major axis at position angle  $pa = 99.56^\circ$  at 230 GHz, and  $3.58'' \times 2.57''$  with  $pa = 86.00^\circ$  at 115 GHz. The FWHM of the primary beam of the antennas is  $20.9''$  at 230 GHz and  $41.8''$  at 115 GHz.

## 2.2. ON-OFF spectra

ON-OFF spectra of the CO  $J(2-1)$  line are shown in Fig. 3a. The integration time is 2 minutes (on+off) for each spectrum. They show a feature moving from positive to negative velocities, and to positive velocities again, with respect to the nucleus velocity frame. In other words, a jet-like CO gas feature, which velocity vector with respect to Earth rotated during the course of the observations, is observed. This CO gas feature contributes up to 28% of the total line area.

The synodic rotation period of comet Hale-Bopp in February–April 1997 has been deduced from studies of the dust shells (Sarmecanic et al., 1997; Farnham et al., 1999; Ortiz & Rodríguez, 1999). The most accurate value  $P = 11.31 \pm 0.01$  hr measured by Farnham et al. (1999) is in agreement with a slightly larger sidereal rotation period  $P = 11.34 \pm 0.02$  hr (Licandro et al., 1998; Jorda et al., 1999). Figure 4 plots the evolution of the line velocity shift (the spectrum first order momentum) with time. The points follow a sinusoidal curve which period corresponds to the comet's nucleus rotation (taken to be equal to 11.35 hr throughout this paper). The sinusoid determined from a least-squares fit with fixed period  $P = 11.35$  h has a mean level of  $v_0 = -0.05 \pm 0.01$  km s<sup>-1</sup> and its amplitude is  $\mathcal{A} = 0.29 \pm 0.03$  km s<sup>-1</sup> (Fig. 4). The line area does not show significant variation with time, with a mean value of  $4.22 \pm 0.03$  K km s<sup>-1</sup> in main beam brightness temperature scale  $T_{mB}$  (i.e., 82.8 Jy km s<sup>-1</sup> in flux density scale). Fluctuations of ~10% at most are observed (with a standard deviation of 5%), which are not correlated with the velocity shift variations. The velocity shift curve obtained for the  $J(1-0)$  line is much more noisy (error bars ~0.2 km s<sup>-1</sup> on the individual spectra), but is similar to the  $J(2-1)$  velocity shift curve: a least-squares sinusoid fit with  $P$  fixed to 11.35 h leads to  $\mathcal{A} =$

<sup>1</sup> <http://www.iram.fr/IRAMFR/GILDAS/>

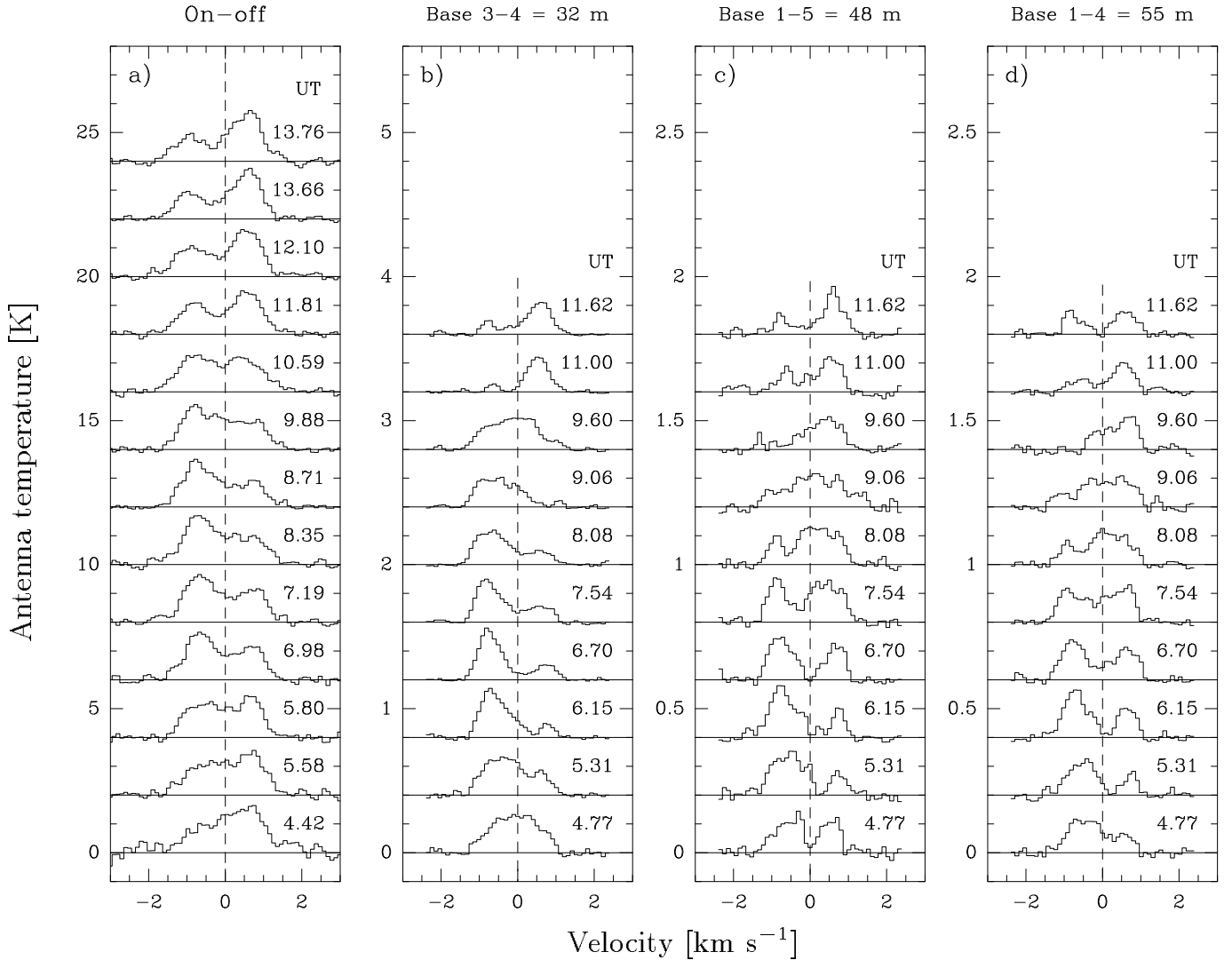


**Fig. 3.** CO  $J(2-1)$  spectra obtained in ON-OFF and interferometric modes as a function of time, given in UT hours on 11 March, 1997. The velocity scale is with respect to the comet rest velocity. Spectra have been shifted vertically according to observation time, but are scaled identically. **a)** ON-OFF spectra: the integration time is 2 min (on+off). **b–d)** Interferometric spectra (visibility amplitude as a function of spectral channel): averages of 25 to 27 scans of 1 min. Only data for the 3 shortest baselines are shown.

$0.39 \pm 0.16 \text{ km s}^{-1}$ ,  $v_0 = -0.05 \pm 0.05 \text{ km s}^{-1}$  (Henry, 2003). Adding all spectra, the mean velocity shift of the  $J(1-0)$  line is  $-0.09 \pm 0.05 \text{ km s}^{-1}$ , in agreement with that of the  $J(2-1)$  line ( $-0.083 \pm 0.007 \text{ km s}^{-1}$ ). The line area of the  $J(1-0)$  line is  $0.552 \pm 0.022 \text{ K km s}^{-1}$  in the  $T_{\text{mB}}$  scale (i.e.,  $10.8 \text{ Jy km s}^{-1}$ ).

From the spin axis orientation and the equatorial coordinates of the comet, it is possible to derive the angle  $\theta_\omega$  (aspect angle) between the spin axis and the line of sight, and the North pole position angle  $pa_\omega$ , defined from North to East. The different spin orientations published in the literature are listed in Table 1.

Adopting the spin orientation derived by Jorda et al. (1999) and Schleicher et al. (2004), the comet spin axis was then only  $20^\circ$  far from the plane of the sky. In such a geometrical configuration, a polar CO jet would lead to an almost constant velocity shift. A jet close to the equator can explain a velocity shift following a sinusoid centred around  $v_0 \sim 0 \text{ km s}^{-1}$ . Both this sinusoidal curve and the constant

CO line area show that the amount of CO gas released in this jet did not vary during nucleus rotation. Given the Sun direction (phase angle of  $46^\circ$ ,  $pa = 160^\circ$ ), this near-equatorial CO jet was active night and day at about the same extent.

From the line areas of the  $J(1-0)$  and  $J(2-1)$  ON-OFF profiles, we derive a CO production rate  $Q_{\text{CO}} = 2.1 \times 10^{30} \text{ s}^{-1}$ . Here, we have assumed a Haser parent molecule distribution for CO, and run our excitation model (Sect. 3) with a kinetic temperature  $T$  of 120 K which agrees with temperature determinations pertaining to the 10 000–20 000 km (radius) coma region sampled by the primary beam of PdBI (Biver et al., 1999a; DiSanti et al., 2001). Using an extended production for CO consistent with the IR observations does not significantly affect the inferred  $Q_{\text{CO}}$ . DiSanti et al. (2001) inferred a total CO production rate (nuclear+distributed) fully consistent with our value. In the following sections, we will assume  $T = 120 \text{ K}$  and a total  $Q_{\text{CO}}$  of  $2 \times 10^{30} \text{ s}^{-1}$ .

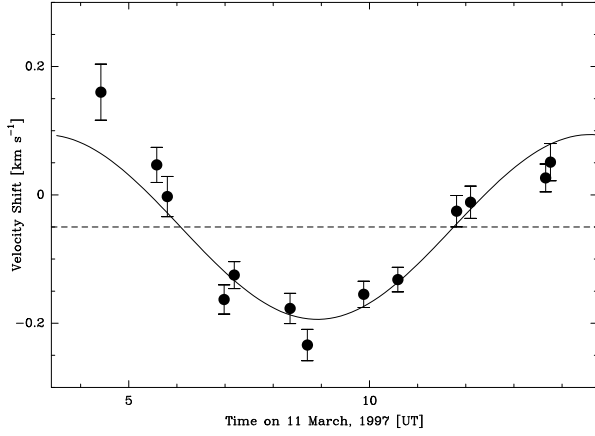


**Fig. 4.** Time evolution of the velocity shift of CO  $J(2-1)$  ON-OFF spectra shown in Fig. 3a. The plotted curve is the least-squares sinusoid fit to the data. It has a fixed period of 11.35 h, an amplitude of  $0.29 \pm 0.03 \text{ km s}^{-1}$ , and a velocity centre  $v_0 = -0.05 \pm 0.01 \text{ km s}^{-1}$  (dotted line).

**Table 1.** Spin axis orientation. Columns 1 and 2 are the equatorial coordinates found in the literature. Columns 3 and 4 are the corresponding position angle ( $pa_\omega$ ) and aspect angle ( $\theta_\omega$ ) on 11 March, 1997.

$\alpha_\omega$	$\delta_\omega$	$pa_\omega$	$\theta_\omega$	Epoch	Ref. <sup>a</sup>
$30^\circ$	$45^\circ$	$66^\circ$	$143^\circ$	May–Nov 1996	[1]
$170^\circ$	$-40^\circ$	$272^\circ$	$9^\circ$	May–Nov 1996	[2]
$240^\circ$	$-56^\circ$	$224^\circ$	$53^\circ$	May–Nov 1996	[2]
$275^\circ$	$-50^\circ$	$217^\circ$	$74^\circ$	Mar–Nov 1996	[3]
$320^\circ$	$-60^\circ$	$189^\circ$	$78^\circ$	Sep 1995–Jan 1998	[4]
$290^\circ$	$-40^\circ$	$215^\circ$	$88^\circ$	Sep 1996–May 1997	[5]
$290^\circ$	$-60^\circ$	$203^\circ$	$72^\circ$	Feb 18, 1997	[6]
$255^\circ$	$-60^\circ$	$216^\circ$	$59^\circ$	Feb 1997	[2]
$275^\circ$	$-57^\circ$	$211^\circ$	$68^\circ$	Feb–Mar 1997	[7]
$276^\circ$	$-54^\circ$	$213^\circ$	$71^\circ$	Apr 1996–May 1997	[8]

<sup>a</sup> [1] : Sekanina et al. (1997), [2] : Sekanina & Boehnhardt (1999), [3] : Licandro et al. (1999), [4] : Biver et al. (1998), [5] : Metchev & Luu (1998), [6] : Vasundhara & Chakraborty (1999), [7] : Jorda et al. (1999), [8] : Schleicher et al. (2004).

### 2.3. Interferometric data

We present in Fig. 5 the line integrated maps of CO  $J(2-1)$  and  $J(1-0)$ . 8 hours of observations were averaged (from 4.5 h UT to 12.5 h UT) and 25 velocity channels (12 on both sides the central channel corresponding to the nucleus velocity) were co-added. An asymmetrical shape, which is not aligned with the elliptical clean beam (the synthesized interferometer beam), is observed and related to the anisotropy of the gas emission.

In the line integrated interferometric map of CO  $J(2-1)$  (Fig. 5), the position of the peak brightness ( $C_m$ ) is at RA = 22h30m38.02s and Dec =  $40^\circ 46' 3.1''$  (with an astrometric precision of  $0.07''$ ) in apparent geocentric coordinates given for 7.00 h UT. The peak position of the CO  $J(1-0)$  brightness (RA = 22h29m38.46s and Dec =  $40^\circ 41' 10.1''$  at 4.00 h UT) is consistent with that of  $J(2-1)$ , taking into account the comet motion from 4 to 7 h

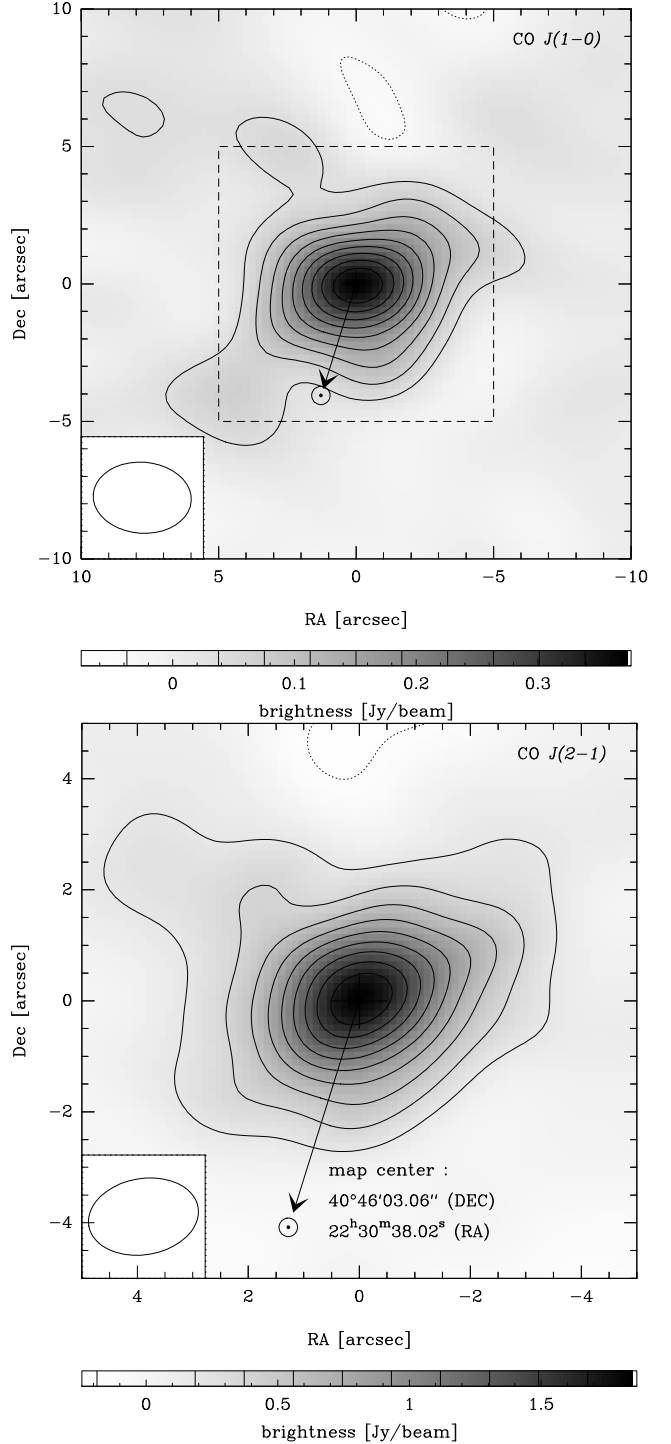


**Fig. 5.** CO  $J(1-0)$  (top) and  $J(2-1)$  (bottom) line integrated maps observed on 11 March, 1997 (all data). 25 spectral channels have been averaged. The synthesized beam is in the lower left. The dashed square on the  $J(1-0)$  map corresponds to the size of the  $J(2-1)$  map. For the CO  $J(1-0)$  line, contours are  $0.037 \text{ Jy/beam}$ , and the r.m.s. is  $0.018 \text{ Jy/beam}$ . For the  $J(2-1)$  line, contours are  $0.186 \text{ Jy/beam}$  and the r.m.s. is  $0.066 \text{ Jy/beam}$ . Iso-contours are successive multiples of 10% of the maximum intensity, at 10 to 100 % of the maximum intensity. The solar direction is indicated. The original images have been shifted so that the maximum brightness peaks at the centre of the maps. In units of line area, the intensities at maximum brightness are  $0.93 \pm 0.04$  and  $4.65 \pm 0.15 \text{ Jy km s}^{-1}$  for the  $J(1-0)$  and  $J(2-1)$  lines, respectively.

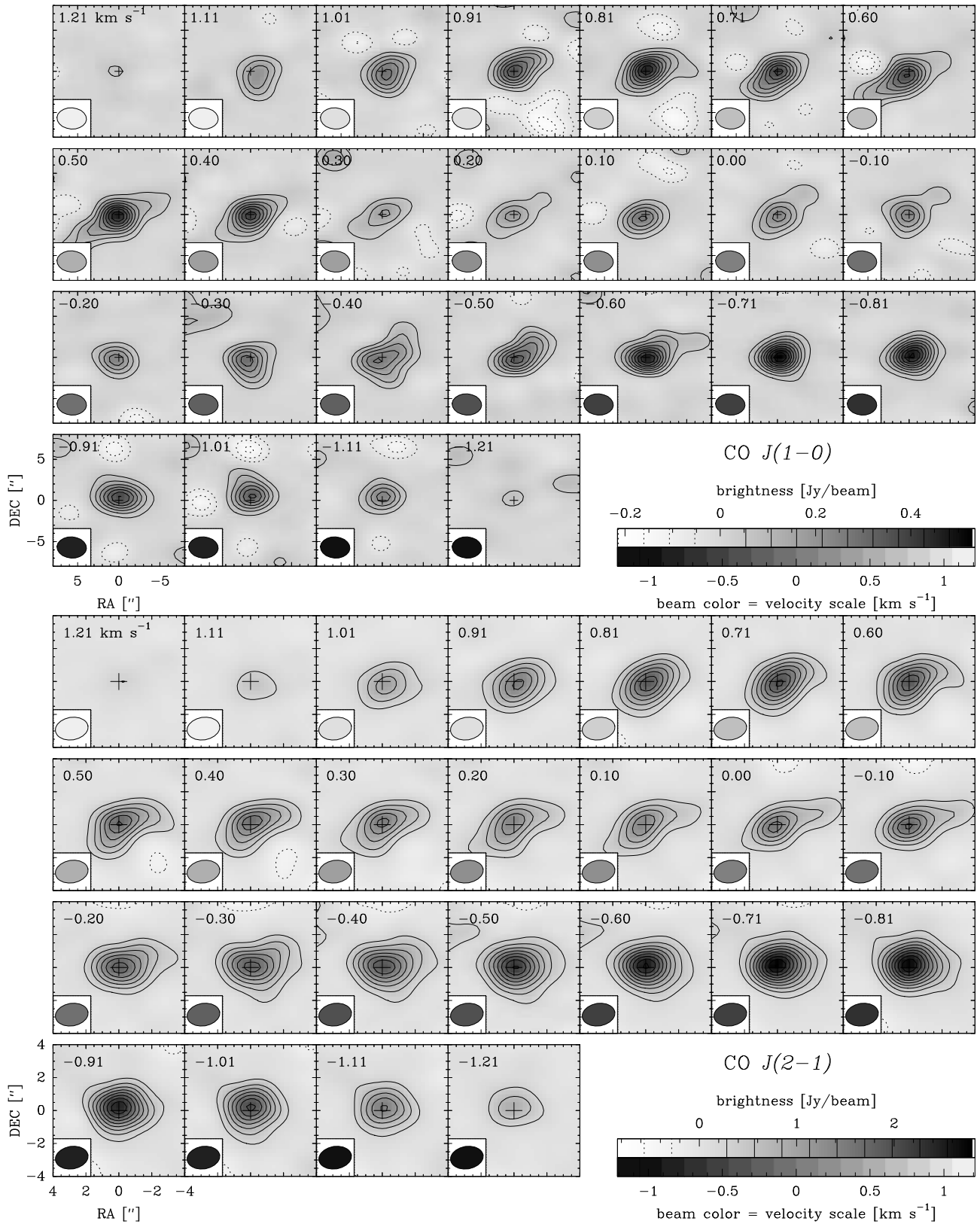


**Fig. 6.** CO maps as a function of spectral channel on 11 March, 1997 (all data averaged). RA and Dec positions are with respect to the mean photometric centre  $C_m$  determined from the whole data set. The velocity (with respect to the comet rest velocity) of the spectral channels is indicated in the top left corner of the maps. The synthesized beam is in the lower left, and is coloured according to the velocity value.  $J(1-0)$  line (top): contour interval is 0.053 Jy/beam and the r.m.s. is 0.046 Jy/beam.  $J(2-1)$  line (bottom): contour interval is 0.283 Jy/beam and the r.m.s. is 0.15 Jy/beam. Contours correspond to multiples of 10% the peak flux density measured on channels at Doppler velocities of  $-0.71$  and  $-0.81 \text{ km s}^{-1}$ .

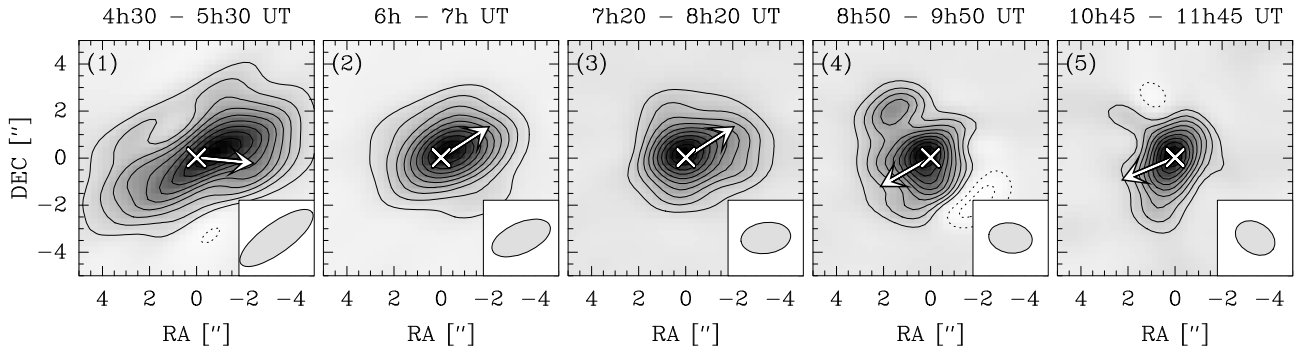


**Fig. 7.** Individual maps of CO  $J(2-1)$  for data subsets of 1 h. Iso-contours are successive multiples of 10% of the maximum intensity, at 10 to 100 % of the maximum intensity. For each map labelled (i) on the top left corners, a cross locates the mean photometric centre  $C_m$  determined from the whole data set. The arrow represents the direction of the individual photometric centre  $C_i$  with respect to  $C_m$ .  $C_i$  is evaluated by fitting a 2-D Gaussian of adjustable width. The beam shape is shown in the bottom right corner.

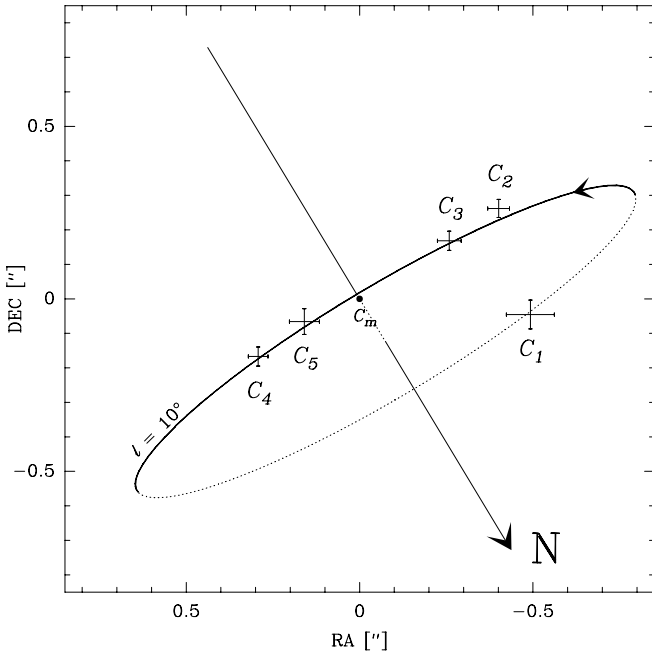


**Fig. 8.** Time evolution of the photometric centres. Photometric centres  $C_i$ , with  $i$  referring to the maps shown in Fig. 7, are given with their errorbars. The ellipse drawn is a least-squares fit to the data. It corresponds to a parallel of latitude  $10^\circ$  North of a sphere, with spin axis aspect angle =  $80^\circ$  and position angle =  $211^\circ$ .

UT (see Boissier et al., 2007). The peak position of the continuum emission at 230 GHz observed simultaneously also almost coincides ( $0.2''$  offset) with the CO  $J(2-1)$  peak (Altenhoff et al., 1999; Boissier et al., 2007). Using orbital elements based on optical astrometric positions from April 1996 to August 2005 (JPL solution 220), the offset between the CO peak and the ephemeris is  $+2.9''$  in Dec and  $+0.4''$  in RA. So, positions of the CO and radio continuum brightness peaks differ by typically  $+3''$  in Dec from optical astrometric positions. A bright dusty jet was identified southward in the optical images of comet Hale-Bopp near perihelion (e.g., Jorda et al., 1999). As shown by Boissier et al. (2007), the optical astrometric positions were more af-

ected by dusty jets than the radio positions. Boissier et al. (2007) showed that the astrometric positions provided by the IRAM continuum radio maps provides an orbit which does not require the existence of non-gravitational forces acting on the Hale-Bopp nucleus, in contrast to those derived from only optical positions, thereby solving a contentious issue. In conclusion, there is no substantial offset between the nucleus position and the mean photometric centre of CO emission.

The  $J(1-0)$  and  $J(2-1)$  spectral channel maps (Fig. 6) were obtained with the same procedure. The peak brightness on the blue channels is stronger than that on the red ones. This indicates more emission toward the Earth and is related to the jet seen in ON-OFF spectra. Indeed, the interferometric observations covered only 2/3 of the nucleus rotation period, when the jet was, most of the time, facing the Earth (Fig. 4). The spectral maps show that the CO coma structure is complex. The interpretation of the brightness distribution on these maps is not straightforward, since the signal is here averaged over the entire period of observation and the CO coma is rotating. The most central channels are sensitive to molecules expanding along directions close to the plane of the sky. They show coma structures towards North-West and South-East quadrants (roughly along a direction perpendicular to the projected rotation axis, see the 230 GHz maps in Fig. 6). These structures may trace the jet at the time it was near the plane of the sky. Channels at high negative velocities ( $-0.6$  to  $-0.9$  km s $^{-1}$ ) show a much brighter and strongly peaked intensity distribution because the jet is here facing the Earth.

In order to investigate whether there is temporal evidence for the rotating jet in the images of the CO emission, we have combined the data into five parts of about 1 hour each. Resulting maps are presented in Fig. 7. Because of Earth rotation, the beam shape rotates with time from map to map and changes dimension (see next paragraph). This prevents a detailed study of the rotating jets directly from the maps and, as explained later, another approach will be used. However, an interesting feature is observed. From the observations averaged over the whole day, we have derived the mean photometric centre of CO emission,  $C_m$ . For each map  $i$ , we can also derive the photometric centre,  $C_i$ , and the vector  $\mathbf{J}_i = \overrightarrow{C_m C_i}$ , as shown in Fig. 7. The time evolution of  $\mathbf{J}_i$  is presented in Fig. 8. We observe that it moves counterclockwise (disregarding  $C_5$ ) along an ellipse which

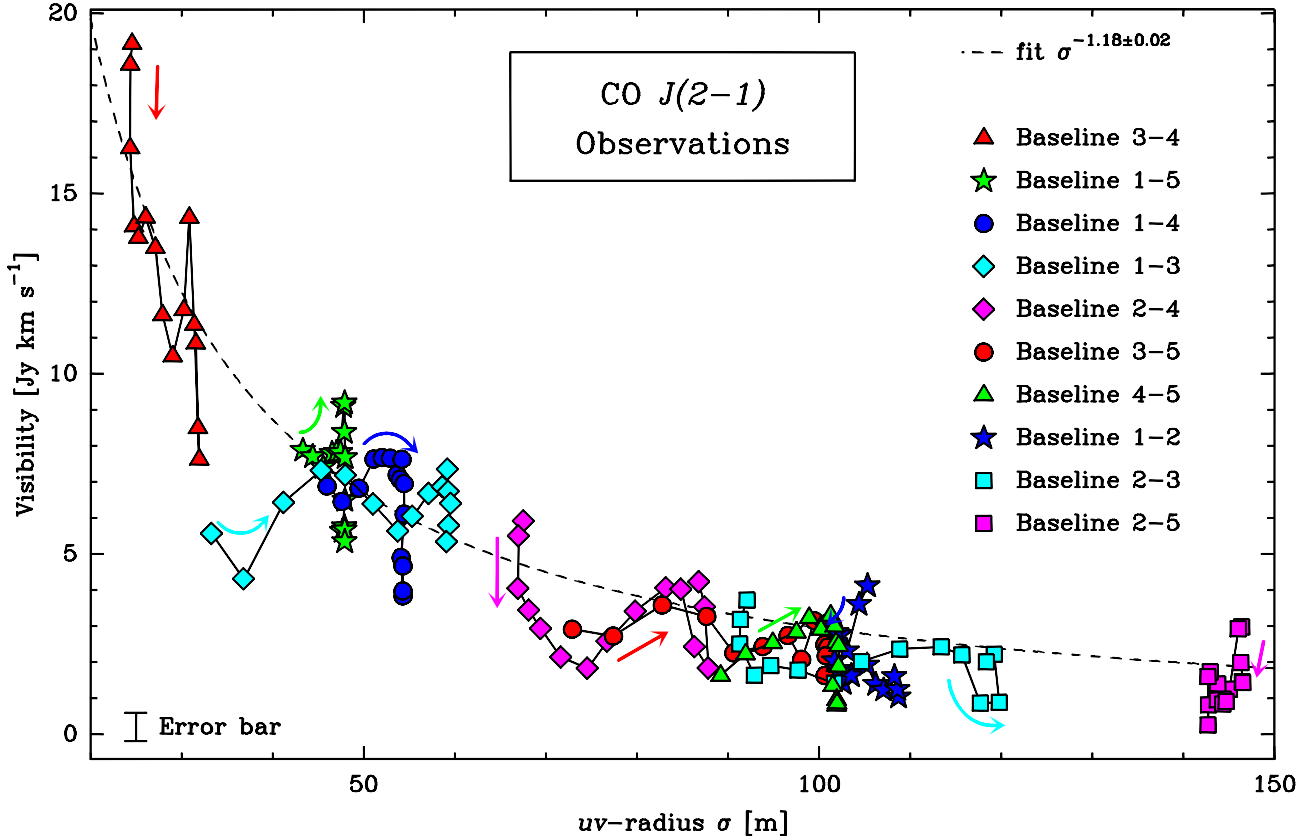


**Fig. 9.** Time evolution of the visibility amplitudes with respect to the  $uv$ -radius  $\sigma$ . Different symbols are used for the different baselines. For some baselines, the arrow shows the direction of time evolution of the  $uv$ -radius. The uncertainties on the data points due to thermal and phase noise range from 0.29 to 0.65 Jy km s<sup>-1</sup>. Phase noise affects the uncertainties by 2% (short baselines) to 10% (long baselines). The mean error bar ( $\pm 0.40$  Jy km s<sup>-1</sup>) is quoted on the figure. The dashed curve is a least-squares fit of a power law to the data.

long axis is perpendicular to the spin axis direction. Such a displacement is that expected in presence of a CO rotating jet. Provided  $C_m$  coincides with the nucleus position,  $\mathbf{J}_i$  reflects the jet direction on map  $i$ . For a spherical nucleus and constant jet activity, the  $C_i$ 's locus should be then an ellipse which long axis position angle is perpendicular to the spin axis, the other characteristics of the ellipse (axis lengths, centroid) being related to the amount of CO gas inside the jet, as well as to its latitude on the nucleus surface. A least-squares fit of the photometric centres leads to an ellipse (Fig. 8) that corresponds to a spin axis with position angle  $pa_\omega = 211^\circ$  and aspect angle  $\theta_\omega = 79^\circ$ , in good agreement with most of the published values (Table 1). The ellipse dimensions and position inferred from the fit do not provide direct quantitative information on the jet relative strength and latitude because the nucleus position may be off by a fraction of an arcsec with respect to  $C_m$ . However, the significant displacement of the photometric centre during nucleus rotation excludes a high-latitude jet, in agreement with the conclusion obtained from the ON-OFF spectra. The small offset between  $C_m$  and the nucleus position (as determined from the peak of the continuum emission) is also consistent with a low-latitude jet.

For a deeper study of the interferometric data, we have decided to work on complex visibilities in the  $uv$ -plane. For readers not familiar with interferometry, let us explain briefly what this means and how maps are obtained. An

interferometer measures the Fourier transform (FT) of the source brightness distribution on the sky. The complex visibilities  $\mathcal{V}(u, v)$  sample the FT at points  $(u, v)$  in the Fourier plane, also called the  $uv$ -plane. These points are the projections of the baselines onto the plane of the sky and define the  $uv$ -coverage of the observations (Fig. 2). As the Earth rotates, the locus of the points  $(u, v)$  produced by one baseline is an arc of ellipse. Therefore, the  $uv$ -radius  $\sigma = \sqrt{u^2 + v^2}$  changes with time (except if the source observed is circumpolar, because the locus is then a circle). The longer we observe, the longer are these arcs, the larger is the  $uv$ -plane coverage (see Thompson et al., 1991, chap. 4, §4.2). (In fact, the  $uv$ -coverage produced by a couple of antennas comprises two arcs of ellipse symmetrical with respect to the centre  $(u, v) = (0, 0)$ ; this is because the source brightness distribution is a real function, so its FT verifies  $\mathcal{V}(u, v) = \mathcal{V}(-u, -v)$ .) In order to make a map, one has first to compute the inverse Fourier transform of the sampled signal. In a second time, this *dirty map* is deconvolved from the *dirty beam*, which is the FT of the  $uv$ -coverage. Because the  $uv$ -plane is not regularly covered, interpolations are made when performing the FT. In addition, when the  $uv$ -coverage is highly anisotropic, the dirty beam presents intense sidelobes, which might not be properly accounted for in the deconvolution step. This might result in the apparition of artefacts. The anisotropic  $uv$ -coverage also results in an elliptical clean beam.



Since the individual baselines have different directions and lengths, they probe different scales and regions of the coma. So, visibilities have to be studied for each baseline separately. We plot in Fig. 9 the time evolution of the visibility amplitude  $\mathcal{V}$  of the CO  $J(2-1)$  line with respect to the  $uv$ -radius  $\sigma$ . The visibilities have been integrated over velocity and have units of line area. Let us assume that the line is optically thin and its excitation does not vary within the field of view. For an isotropic coma described by a parent molecule distribution, the visibility curve would follow  $\mathcal{V}(\sigma) \propto \sigma^{-1}$ , provided the photodissociation scale length is large compared to the field of view, which is the case here (Bockelée-Morvan & Boissier, 2009). We observe in Fig. 9 some modulations with respect to the mean evolution (in  $\sigma^{-1.18}$ ) that are not due to noise. They cannot be due to variations of the activity of the comet since the area of the line, observed in ON-OFF mode, is roughly constant with time. Furthermore, modulations do not present the same behaviour from one baseline to another.

We presented in Fig. 3b–d spectra issued from the three shortest baselines of the interferometer. As on the ON-OFF spectra (Fig. 3a), we can see spectral features moving from red to blue velocities. Figure 10 presents the time evolution of the interferometric velocity shifts. At least for the five shortest baselines, they can be fitted by sinusoids of period equal to the nucleus rotation period. We observe that these curves are not in phase. As the baselines do not have the same length, nor the same orientation, this phase difference may suggest that the CO jet is spiralling and detected at different times with the various baselines. A straight jet would produce velocity shift curves in phase.

The next section presents a model with a rotating gas jet aimed at the interpretation of these data.

### 3. Model

The model is a static 3-dimensional model simulating a spiralling gas jet. It computes  $uv$ -tables (i.e., visibilities) corresponding to the observational conditions of the data, that is with the same  $uv$ -coverage. The time evolution of the coma is simulated by computing a serie of successive static  $uv$ -tables.

The CO coma is modelled as a combination of an isotropic outgassing and a gas jet defined by:

- its half-width  $\Psi$ ;
- its latitude  $\ell$  on the nucleus, assumed to be spherical;
- the fraction  $f_{\text{CO}}$  of the CO released within the jet.

The model parameters are summarized in Table 2.

The coordinate frame ( $Oxyz$ ) used in the calculations has its origin at the comet nucleus with the  $z$ -axis along the line of sight opposite to the Earth, and the  $x$  and  $y$ -axes pointing East and North in the plane of the sky.  $r_0$  is the nucleus radius. The jet direction at the nucleus surface  $\mathbf{J}_0$  is  $(\theta_0, \phi_0)_t$  in the ( $Oxyz$ ) frame at time  $t$  (usual spherical coordinates) and is moving with time due to the nucleus rotation. Let us define  $\mathbf{R}_\omega$  the rotation matrix for a lapse  $\Delta t$ , so that we have  $(\theta_0, \phi_0)_{t+\Delta t} = \mathbf{R}_\omega \cdot (\theta_0, \phi_0)_t$ . The jet direction at distance  $r = r_0 + v_{\text{exp}}\Delta t$  in the coma is  $\mathbf{J}_r = \mathbf{R}_\omega^{-1} \cdot \mathbf{J}_0$ , where  $v_{\text{exp}}$  is the gas expansion velocity.

We assume a Haser-like parent molecule distribution for CO. Indeed, as commented in Sect. 1, though infrared observations suggest that part of the CO in Hale-Bopp coma is

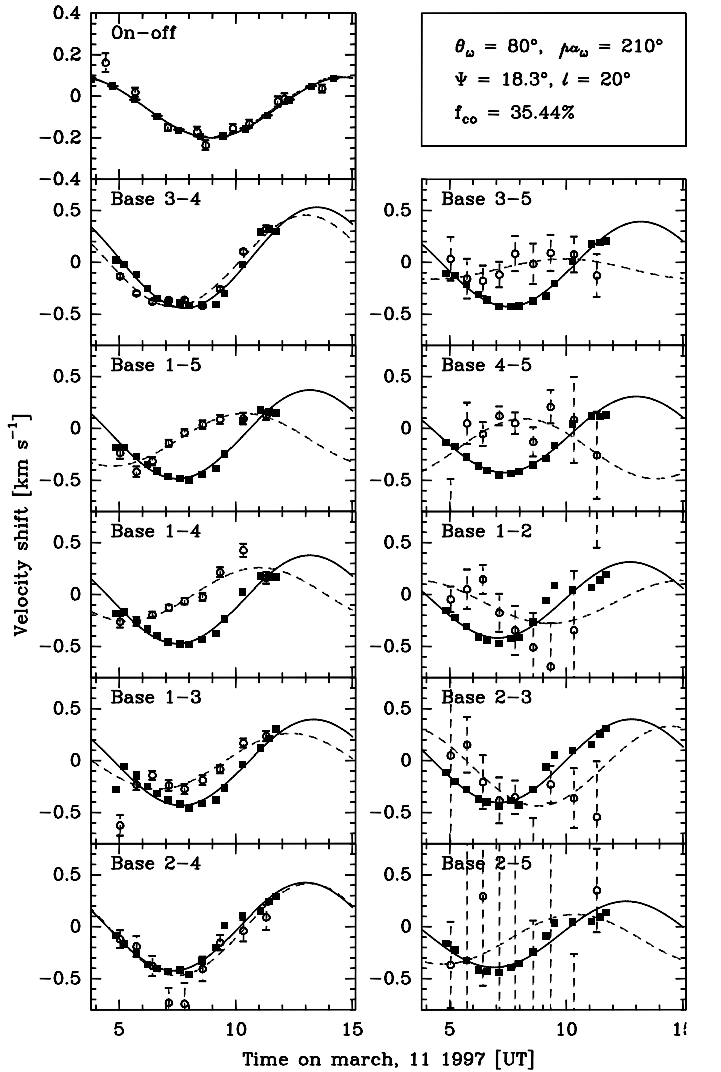


**Fig. 10.** Time evolution of the CO  $J(2-1)$  velocity shifts and fitted sinusoids. Baselines are indicated in the top left corners. Observations are shown with empty circles with error bars, and dashed curves for the sinusoids. Model results (plain squares and plain curves) are for parameter set (3) of Table 3 with  $pa_\omega = 210^\circ$  ( $\theta_\omega = 80^\circ$ ,  $\Psi = 18.3^\circ$ ,  $\ell = 20^\circ$  and  $f_{\text{CO}} = 35.5\%$ ).

originating from a distributed source (DiSanti et al., 2001; Brooke et al., 2003), the present observations do not require CO to be extended (Bockelée-Morvan & Boissier, 2009). The local density at  $(r, \theta, \phi)$  direction is then given by:

$$n_{\text{CO}}(r, \theta, \phi) = \frac{Q(r, \theta, \phi)}{4\pi r^2 v_{\text{exp}}} \exp\left(-\frac{(r - r_0)}{L_{\text{CO}}}\right), \quad (1)$$

where

$$Q(r, \theta, \phi) = Q_{\text{iso}} + 4\pi Q_{\text{jet}} \mathcal{G}(r, \theta, \phi). \quad (2)$$

$Q_{\text{iso}}$  and  $Q_{\text{jet}}$  are the total CO production rates due to the isotropic contribution and within the jet, respectively. For the sake of simplicity, the total CO production rate  $Q_{\text{CO}} = Q_{\text{iso}} + Q_{\text{jet}}$  is fixed, and taken to be equal to the  $2 \times 10^{30}$

$s^{-1}$  (Biver et al. (1999a), see Sect. 2.2).  $f_{\text{CO}} = \frac{Q_{\text{jet}}}{Q_{\text{CO}}}$  is a free parameter. The function  $\mathcal{G}(r, \theta, \phi)$  describes the jet pattern and is a normalized Gaussian ( $\int \mathcal{G}(\Omega) d\Omega = 1$ ) of half width  $\Psi$  centred on  $\mathbf{J}_r$ .  $L_{\text{CO}} = v_{\text{exp}}/\beta_{\text{CO}}$  is the photodissociative scalelength, where  $\beta_{\text{CO}}$  is the CO photodissociation rate.

The code uses  $N = 47$  ( $Oxy$ ) grids, each of them sampling one channel of the spectrum centred on  $v_i = (\frac{N+1}{2} - i) \delta v$ , in the nucleus velocity frame, with  $\delta v = 0.10 \text{ km s}^{-1}$ . The ( $Oxy$ ) grids are  $100'' \times 100''$  long<sup>2</sup>. They are divided into  $256 \times 256$  cells which dimensions are  $(\delta x, \delta y)$  ( $\delta x = \delta y = 0.39''$ ).

In the optically thin case, the brightness distribution in the plane of the sky [ $\text{W m}^{-2} \text{ sr}^{-1}$ ], when selecting only molecules contributing to channel  $i$ , is given by:

$$F_i(x, y) = \frac{\mathcal{N}_i(x, y)}{\delta x \delta y} h\nu A_{ul} \frac{1}{4\pi \Delta^2}, \quad (3)$$

where  $\nu$  is the line frequency, and  $A_{ul}$  is the Einstein coefficient for spontaneous emission.  $\delta x$  and  $\delta y$  have units of radians.  $\Delta$  is the geocentric distance.

$\mathcal{N}_i(x, y)$  is the number of CO molecules in the upper state of the transition sampled by the cells with Doppler velocities contributing to channel  $i$ :

$$\mathcal{N}_i(x, y) = \int_{x-\frac{\delta x}{2}}^{x+\frac{\delta x}{2}} \int_{y-\frac{\delta y}{2}}^{y+\frac{\delta y}{2}} \int_{-10 L_{\text{CO}}}^{10 L_{\text{CO}}} n_{\text{CO}} p_u \text{H}_i dx dy dz, \quad (4)$$

where  $p_u$  is the relative population of the upper level of the transition, which depends on the radial distance to nucleus, and  $n_{\text{CO}}$  is from Eq. 1.  $\text{H}_i$ , the function used to select velocities, is defined by:

$$\text{H}_i(x, y, z) = \begin{cases} 1 & \text{if } v_z(x, y, z) \in [v_i - \frac{\delta v}{2}; v_i + \frac{\delta v}{2}] \\ 0 & \text{elsewhere} \end{cases} \quad (5)$$

where  $v_z(x, y, z)$  is the gas velocity projected onto the line of sight. The gas velocity is radial, and its amplitude is a Gaussian centred on  $v_{\text{exp}}$ , which width is  $2\sqrt{\ln(2)kT/m}$ , to account for thermal broadening.  $k$  is the Boltzman constant,  $T$  the kinetic temperature and  $m$  the CO molecular mass.

Because the CO production rate is high in comet Hale-Bopp and a dense CO jet is present, optical depth effects need to be considered for the calculation of the CO  $J(2-1)$  brightness distribution (i.e.,  $F_i(x, y)$ ). They are not expected to affect significantly the ON-OFF spectra, but could be significant for the interferometric signals. The results presented in this paper were performed solving the full radiative transfer equation, as explained in Boissier et al. (2007), assuming the local velocity dispersion to be thermal.

A synthetic 47-channels ON-OFF spectrum is obtained by the convolution of  $F_i$  with the antennas primary beam.

For each channel  $i$ , the visibilities are defined by (see e.g., Thompson et al., 1991, chap. 4, §4.1) :

$$\mathcal{V}_i(\boldsymbol{\sigma}) = \frac{c}{\nu \delta v} \int_{4\pi} A(\mathbf{s}) F_i(\mathbf{s}) \exp\left(-\frac{2i\pi\nu}{c} \boldsymbol{\sigma} \cdot \mathbf{s}\right) d\Omega, \quad (6)$$

<sup>2</sup> this is much larger than the primary beam of the antennas, but this was necessary in order to have a good resolution in the Fourier plane.

**Table 2.** Model parameters.

fixed parameters		
heliocentric distance	$r_h$	0.989 AU
geocentric distance	$\Delta$	1.368 AU
gas expansion velocity <sup>(a)</sup>	$v_{\text{exp}}$	1.05 km s <sup>-1</sup>
total CO production rate <sup>(a)</sup>	$Q_{\text{CO}}$	$2.0 \times 10^{30} \text{ s}^{-1}$
CO photodissociation rate <sup>(b)</sup>	$\beta_{\text{CO}}$	$7.50 \times 10^{-7} r_h^{-2}$
nucleus rotation period	$P$	11.35 h
free parameters		
fraction of CO in the coma outgassed in the jet		$f_{\text{CO}}$
jet latitude		$\ell$
jet half-width		$\Psi$
rotation axis aspect angle		$\theta_\omega$
rotation axis position angle		$pa_\omega$

<sup>(a)</sup> Biver et al. (1999a)

<sup>(b)</sup> Huebner et al. (1992)

where  $\boldsymbol{\sigma}$  is the baseline vector for two antennas, with coordinates  $(u, v)$  in the  $uv$ -plane.  $\mathbf{s}$  is a vector in the sky plane which coordinates are  $(x, y)$  in radian units.  $A$  is the power pattern of the antennas, and  $d\Omega$  is an element of solid angle on the sky.  $\mathcal{V}_i(\boldsymbol{\sigma})$  is here in units of [ $\text{W m}^{-2} \text{ Hz}^{-1}$ ] or janskys. Equation 6 can be approximated to :

$$\mathcal{V}_i(u, v) = \frac{c}{\nu \delta v} \int_{-\infty}^{+\infty} \int_{-\infty}^{+\infty} A(x, y) F_i(x, y) \times \exp\left(-\frac{2i\pi\nu}{c}(ux + vy)\right) dx dy. \quad (7)$$

Visibilities are computed with a Fast Fourier Transform (FFT) algorithm.

The population of the rotational levels ( $p_u$ ) is derived from an excitation model which takes into account collisions with  $\text{H}_2\text{O}$  and IR radiative pumping of the  $v(1-0)$  CO vibrational band (Crovisier & Le Bourlot, 1983; Crovisier, 1987). This model provides populations  $p_u$  as a function of radial distance  $r$ , given a  $\text{H}_2\text{O}$  density law with  $r$ . For simplicity, we assumed an isotropic  $\text{H}_2\text{O}$  coma, and  $p_u$  only depending upon  $r$ . The collisional CO- $\text{H}_2\text{O}$  cross-section is taken equal to  $\sigma_c = 2 \times 10^{-14} \text{ cm}^2$  (Biver et al., 1999b), and the  $\text{H}_2\text{O}$  production rate is  $Q_{\text{H}_2\text{O}} = 10^{31} \text{ s}^{-1}$  (Colom et al., 1999). In the simulations presented in Sect. 4, a kinetic temperature  $T = 120 \text{ K}$  is used (see Sect. 2.2 for further discussion). The evolution of the population of the CO  $J = 2$  and  $J = 1$  levels is shown in Fig. 11. The beam size of  $20.9''$  for CO  $J(2-1)$  corresponds to  $r \sim 10\,000 \text{ km}$  in the coma. Most CO molecules within the field of view are in local thermal equilibrium.

Given the evolving coma, a full simulation of the observations would require to compute for each one minute scan the visibilities corresponding to the current state of the coma and to their  $uv$ -coverage. In order to limit the computer time, we modelled a whole nucleus revolution ( $P = 11.35 \text{ h}$ ) by 12 snapshots (see Fig. 12). We tested the validity of the approach by verifying that calculations with an increased time sampling (namely 36 snapshots) provide similar results. Between 2 snapshots  $i$  and  $i+1$ , the jet direction changed following  $(\theta_0, \phi_0)_{i+1} = \mathbf{R}_\omega(\theta_0, \phi_0)_i$ , where  $\mathbf{R}_\omega$  is the rotation matrix for a span of  $P/12$ . Providing the initial jet longitude at time  $t$  corresponding to snapshot  $i=1$  is fixed, a composite  $uv$ -table can be computed with the  $uv$ -coverage of the observations. The numerical code computes

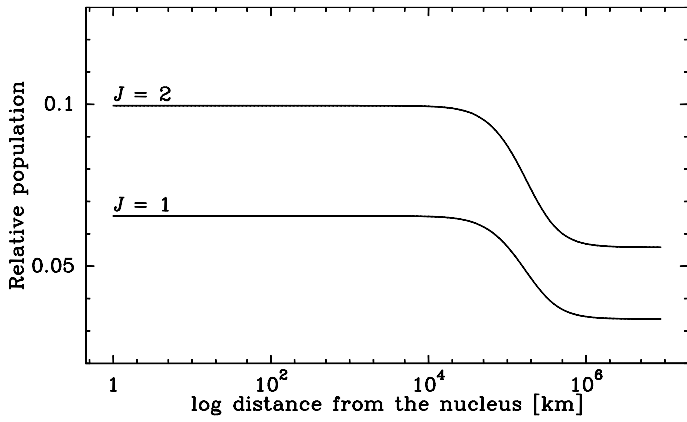


**Fig. 11.** Relative populations of the CO rotational levels  $J = 1$  and  $J = 2$ , as function of distance from the nucleus. A kinetic temperature of 120 K is assumed.

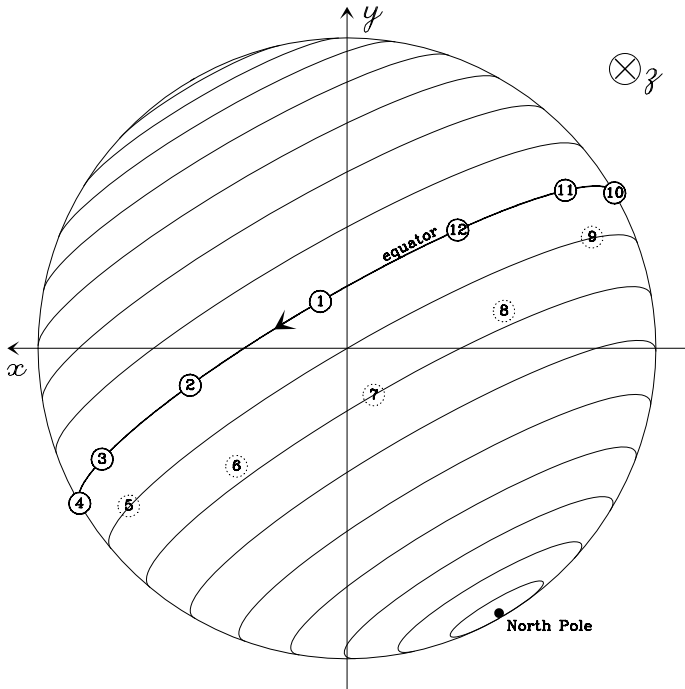


**Fig. 12.** Schematic view of comet Hale-Bopp nucleus on 11 March, 1997, as seen from the Earth assuming  $pa_{\omega} = 210^{\circ}$  and  $\theta_{\omega} = 80^{\circ}$  for the spin orientation. East is on the left. The latitudes are shown by steps of  $10^{\circ}$  and the arrow shows the rotation direction. The symbols represent the series of jet positions used to make a composite  $uv$ -table for an equatorial jet. Plain (respectively dotted) symbols mean that the jet is on the visible (respectively hidden) side of the nucleus.

twelve composite  $uv$ -tables, each of them corresponding to different initial jet longitudes spaced by  $360^{\circ}/12$ . The longitude origin is chosen so that the sub-terrestrial point on the nucleus surface is at a longitude of  $0^{\circ}$ . For illustration, Fig. 12 shows the twelve jet positions for a jet at a longitude of  $0^{\circ}$  at the time of the first snapshot. The model also computes synthetic ON-OFF spectra for each snapshot.

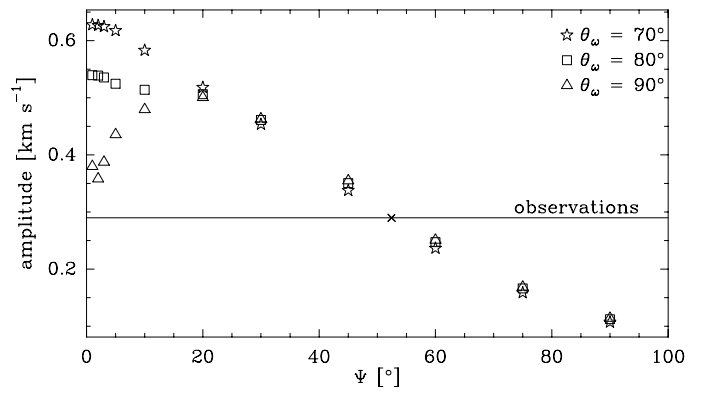


**Fig. 13.** Evolution of the amplitude of the velocity shift curve  $\mathcal{A}$  with  $\theta_{\omega}$  and  $\Psi$ , for  $f_{\text{CO}} = 66\%$  and  $\ell = 0^{\circ}$ . The cross indicates the value of  $\Psi$  required to fit the observations ( $\mathcal{A} = 0.29 \pm 0.03 \text{ km s}^{-1}$ ) for  $\theta_{\omega} = 70\text{--}90^{\circ}$  and  $f_{\text{CO}} = 66\%$ .

## 4. Jet morphology analysis

In this Section, the ON-OFF and interferometric velocity shift curves observed for CO  $J(2-1)$  (Figs 4 and 10), and the time evolution of the visibilities (Fig. 9) will be analysed with the model presented in the previous Section to constrain its free parameters. Because of limited signal-to-noise ratio, it was not possible to make this analysis for  $J(1-0)$  observations. For the spin axis orientation defined by its aspect angle  $\theta_{\omega}$  and position angle  $pa_{\omega}$ , we restricted our study to the mean values found in the literature (see Table 1):  $\theta_{\omega} = 60$  to  $90^{\circ}$ , and  $pa_{\omega} = 200$  to  $230^{\circ}$ . The jet width  $\Psi$  was tested from  $1^{\circ}$  to  $90^{\circ}$ , the jet latitude  $\ell$  from  $0^{\circ}$  to  $90^{\circ}$  North, and  $f_{\text{CO}}$  from 10% to 80%.

### 4.1. ON-OFF velocity shift curve

As discussed in Sect. 2.2, data shown in Fig. 4 are well fitted by a sinusoid with a period  $P = 11.35 \text{ h}$ , an amplitude  $\mathcal{A} = 0.29 \text{ km s}^{-1}$ , and centred on  $v_0 = -0.05 \text{ km s}^{-1}$ . We can also define a phase  $t_0 = 11.75 \pm 0.12 \text{ UT}$ , that corresponds to the time when the velocity shift is equal to  $v_0$  on the increasing side of the curve. We used these three parameters ( $\mathcal{A}$ ,  $v_0$ ,  $t_0$ ) as criterions for selecting the models that could explain the observations. Note that the position angle  $pa_{\omega}$  of the spin axis has no influence on the velocity shift.

The phase  $t_0$  is only ruled by the initial longitude of the jet. From  $t_0$  derived from the observations, the best initial longitude is  $300^{\circ}$  at 3 h 47 UT.

At first order,  $\mathcal{A}$  is governed by  $f_{\text{CO}}$  and  $\Psi$ : it increases when  $f_{\text{CO}}$  increases or  $\Psi$  decreases. This behaviour is easily explained. If  $f_{\text{CO}}$  increases – all other parameters remaining unchanged – there is more signal coming from the jet falling into the same number of spectral channels. Then, the velocity shift increases, so does the amplitude of the velocity shift curve. In a similar way, when  $\Psi$  decreases – keeping  $f_{\text{CO}}$  constant – an equal amount of signal coming from the jet is falling into a larger number of spectral channels. This results in reducing the velocity shift and also  $\mathcal{A}$ . This is illustrated in Figs 13 and 14, which show the evolution of  $\mathcal{A}$  with  $f_{\text{CO}}$  and  $\Psi$ . Moreover,  $\mathcal{A}$  is not sensitive to the aspect angle  $\theta_{\omega}$ , except for small  $\Psi$ 's, as observed in Figs 13 and 14. Furthermore, we note that the jet latitude  $\ell$  has little influence upon the amplitude, within the limits where we tested it ( $|\ell| < 45^{\circ}$ ) (Fig. 15). To conclude, the observed

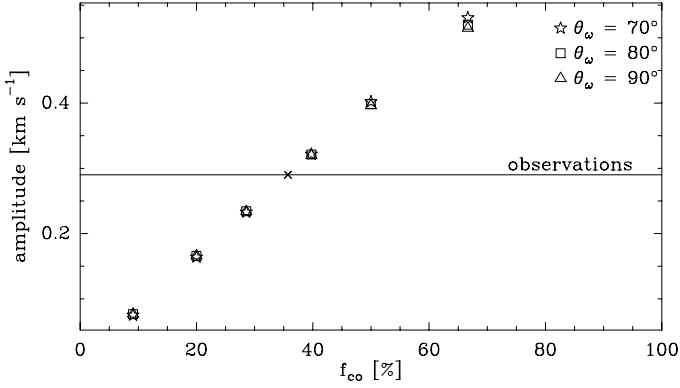


**Fig. 14.** Evolution of the amplitude of the velocity shift curve  $\mathcal{A}$  with  $\theta_\omega$  and  $f_{\text{co}}$ , for  $\Psi = 20^\circ$  and  $\ell = 0^\circ$ . The cross indicates the value of  $f_{\text{co}}$  required to fit the observations ( $\mathcal{A} = 0.29 \pm 0.03 \text{ km s}^{-1}$ ) for  $\theta_\omega = 70\text{--}90^\circ$  and  $\Psi = 20^\circ$ .

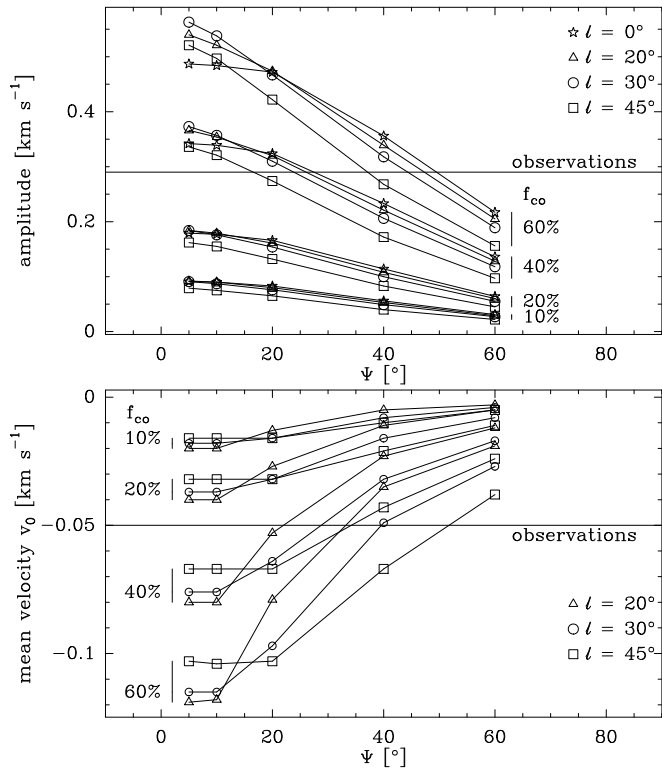


**Fig. 15.** Evolution of  $\mathcal{A}$  (top) and  $v_0$  (bottom) with  $\Psi$  for several  $f_{\text{co}}$  and  $\ell$ . Simulations have been done with  $\theta_\omega = 80^\circ$  and  $pa_\omega = 210^\circ$ . Observed values are  $\mathcal{A} = 0.29 \pm 0.03 \text{ km s}^{-1}$  and  $v_0 = -0.05 \pm 0.01 \text{ km s}^{-1}$ ).

amplitude of  $0.29 \text{ km s}^{-1}$  can be fitted by many  $(f_{\text{co}}, \Psi, \ell)$  combinations.

The mean velocity  $v_0$  of the simulated curves depends mainly on the jet latitude  $\ell$ . An equatorial jet always produces a curve centred on  $0 \text{ km s}^{-1}$ , whatever  $\theta_\omega$ . For  $\theta_\omega < 90^\circ$ , a jet with a northern (resp. southern) latitude produces a curve centred on a negative (resp. positive) velocity. Again, this behaviour is understood. With  $\theta_\omega < 90^\circ$ , the North pole is pointing towards the Earth (see Fig. 12). As a result, a northern jet is more often directed towards the Earth than a southern one. Opposite effects are obtained for  $\theta_\omega > 90^\circ$ , while  $\theta_\omega = 90^\circ$  (rotation axis in the plane of

**Table 3.** Selected sets of parameters  $\theta_\omega$ ,  $\ell$ ,  $\Psi$  and  $f_{\text{co}}$  reproducing the velocity shift curve of the ON-OFF observations.

set	$\theta_\omega$	$\ell$	$\Psi$	$f_{\text{co}}$
(1)	$70^\circ$	$10^\circ$	$19.9^\circ$	35.7%
(2)	$80^\circ$	$10^\circ$	$11.9^\circ$	33.6%
(3)	$80^\circ$	$20^\circ$	$18.3^\circ$	35.5%
(4)	$80^\circ$	$30^\circ$	$33.0^\circ$	47.8%

the sky) always produces a curve centred on  $0 \text{ km s}^{-1}$ , irrespective of the sign of the latitude. The more the rotation axis is far from the plane of the sky, the more the velocity shift curve is shifted. Furthermore, the velocity shift curve is all the more shifted as  $\Psi$  is small and  $f_{\text{co}}$  is large (Fig. 15). This study leads us to the conclusion that, here again, many combinations  $(f_{\text{co}}, \Psi, \ell)$  are able to reproduce the observed  $v_0$ . However, it shows that only a northern jet will be able to fit the observations.

For a given  $(\theta_\omega, \ell, f_{\text{co}})$  parameter set, it is possible to find the jet width  $\Psi$  that is able to reproduce the amplitude  $\mathcal{A} = 0.29 \text{ km s}^{-1}$ . Figure 16 shows in dotted curves the locus of the couples  $(f_{\text{co}}, \Psi)$  that reproduce the right amplitude  $\mathcal{A}$  for several fixed  $(\theta_\omega, \ell)$  values. The same method is employed to determine the couples  $(f_{\text{co}}, \Psi)$  that reproduce the right velocity centre  $v_0 = -0.05 \text{ km s}^{-1}$  (dashed curves in Fig. 16). For each set  $(\theta_\omega, \ell)$ , the intersection of the dotted and the dashed curves gives the only couple  $(f_{\text{co}}, \Psi)$  that reproduces  $\mathcal{A}$  and  $v_0$ . We made these computations for latitudes between  $0^\circ$  and  $45^\circ$ , and for  $\theta_\omega = 70^\circ$  and  $80^\circ$ . Computations for  $\theta_\omega = 90^\circ$  were useless because they provide  $v_0 = 0 \text{ km s}^{-1}$ .

The combinations  $(\theta_\omega, f_{\text{co}}, \Psi, \ell)$  selected by this study are summarized in Table 3. We note that the jet strength  $f_{\text{co}}$  is typically between 35 and 50%. The jet is located on the northern hemisphere at a latitude between  $0^\circ$  and  $45^\circ$  (both excluded) for  $\theta_\omega = 80^\circ$ , and between  $0^\circ$  and  $20^\circ$  (both excluded) for  $\theta_\omega = 70^\circ$ .

The velocity shift curve obtained for parameter set (3) is shown in Fig. 10, together with the observed curve. We note the almost perfect match between model and observations. The corresponding synthetic line profiles are shown in Fig. 17. At any time, the jet contributes to both blue and red channels, with varying relative contributions, due to its spiral shape.

#### 4.2. Interferometric velocity shift curves

In this Section, we study the velocity shift curves observed for the individual baselines. Figure 10 shows model results with the parameter set (3) ( $\theta_\omega = 80^\circ$ ,  $pa_\omega = 210^\circ$ ,  $\Psi = 18.3^\circ$ ,  $\ell = 20^\circ$  and  $f_{\text{co}} = 35.5\%$ ; Table 3). Other parameter sets of Table 3 give similar curves. Modelled curves are periodic functions, with a period equal to  $P$ . They mimic sinusoidal curves, though significant deviations from a sinusoid are observed. This is because line shifts measured on  $\mathcal{V}(u, v)$  spectra are  $(u, v)$  dependent: stronger jet contrast appears in specific regions due to spatial filtering. Then, due to the combination of Earth and jet rotation, regions with more or less jet contrast are sampled by the individual baselines. Simulations show that these curves evolve toward a true sinusoid when the jet width  $\Psi$  is increasing ( $f_{\text{co}}$  kept constant), due to smaller jet contrast. These curves change

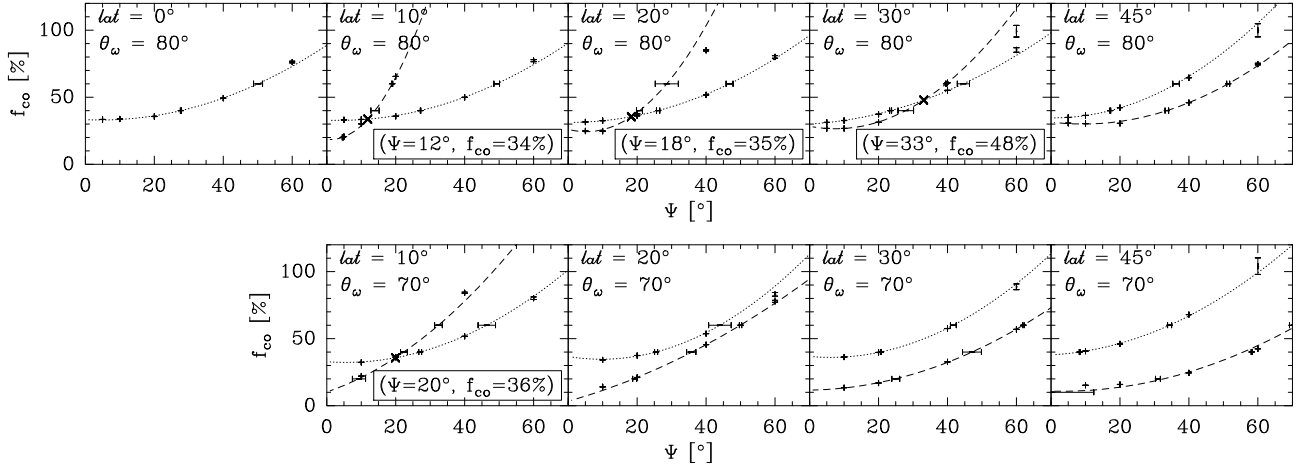


**Fig. 16.** Couples  $(f_{\text{co}}, \Psi)$  that reproduce the amplitude  $\mathcal{A} = 0.29 \pm 0.03 \text{ km s}^{-1}$  (dotted curves) and the mean velocity  $v_0 = -0.05 \pm 0.01 \text{ km s}^{-1}$  (dashed curves) for several couples of  $(\theta_\omega, \ell)$ . The intersections of the curves give, for each  $(\theta_\omega, \ell)$  combination, the only couple  $(f_{\text{co}}, \Psi)$  that reproduces  $\mathcal{A}$  and  $v_0$ .

when varying the jet parameters in the same way than does the ON-OFF curve. Changing the spin axis parameters by  $\pm 10^\circ$  does not affect much the curves.

The modelled velocity shift curves for the different baselines are not in phase, with  $t_0$  (defining the phase, see Sect 4.1) increasing with decreasing baseline length (Fig. 18). We expect a phase offset due to the spiral shape of the jet. Indeed, with respect to long baselines, short baselines probe molecules in more distant regions of the spiral. Hence, they sample molecules released in average at earlier times. In addition, baselines of different length (even if they are parallel) record the maximum signal from the jet at different times due to the curvature of the jet. This can be understood from Fig. 19, which plots the amplitude of the visibility as a function of the orientation and length of the baselines for a simple geometry (rotation axis along the line of sight and equatorial jet) and at a given time. The combination of both effects introduces a phase offset in the velocity shift curves. The delay between two baselines in the velocity shift curves represents the elapsed time between the jet detection by one baseline and its detection by the following one. Note that, given the large curvature of the spiral (molecules travel  $r \sim 10^4 \text{ km}$  when the nucleus rotates by  $90^\circ$ ), only its innermost part contributes significantly to the detected signal. The dashed curve in Fig. 18 shows the evolution of  $t_0$  with  $uv$ -radius, assuming that  $t_0$  varies linearly with  $\sigma/v_{\text{exp}}$ : it follows approximately the  $t_0$  curve computed by the model (plain curve).

The comparison between modelled and observed phases  $t_0$  and amplitudes  $\mathcal{A}$  shows that there is relatively good agreement for some baselines and strong discrepancies for others (Fig. 18). Good agreement for both  $t_0$  and  $\mathcal{A}$  is obtained for baselines 3-4 and 2-4. Phase  $t_0$  is well reproduced for baseline 1-3 (but not the amplitude). Strong discrepancy (by 3 h for  $t_0$  and a factor of almost 2 in  $\mathcal{A}$ ) is observed for baselines 1-4, 1-5 and possibly 4-5 (errorbars are large for this baseline). It is striking to note that good agreement is obtained for baselines with their field of view aligned along the spin vector, while discrepancies are observed for baselines with their field of view perpendicular to the spin vector. Clearly our model is too simple to reproduce all observational characteristics. We did not find any simple explanation for these discrepancies. Velocity accel-

eration inside the jet changes  $t_0$  evolution with baseline in the opposite way: it would result in a flatter increase with decreasing baseline length than obtained with a constant velocity. The presence of other CO evolving structures in Hale-Bopp coma is the likely explanation (Sect. 4.5).

#### 4.3. Visibilities

Figure 9 shows the time evolution of the visibilities  $\bar{\mathcal{V}}$  plotted as a function of the  $uv$ -radius  $\sigma$  (as defined in Sect. 2.3,  $\bar{\mathcal{V}}$  refers to the amplitude of the visibilities integrated over velocity). A least-squares fit to these data gives  $\bar{\mathcal{V}}(\sigma) \propto \sigma^{-1.18 \pm 0.02}$ , to be compared to the  $\sigma^{-1}$  variation expected for a parent molecule distribution and an optically thin line (Bockelée-Morvan & Boissier, 2009). This trend can be explained by optical depth effects being more important for long baselines probing the inner coma.

Modulations are observed around this fit: they trace variations of the brightness distribution sampled by the individual baselines as the baselines and jet are rotating. These modulations are characterized by their shape and their amplitude. The shape depends essentially upon the rotation axis position angle  $pa_\omega$  and the jet latitude  $\ell$ . For example, a high-latitude jet would result in strong modulations for baselines 3-4, 2-4 and 2-3, and no modulations for baselines 1-3 and 1-4 which scan regions along the equator (Fig. 20). The reverse is expected for a high-latitude jet and  $pa_\omega$  at  $90^\circ$  from the nominal  $pa_\omega$  of Hale-Bopp rotation axis. Qualitatively, the observed modulations exclude a high-latitude jet, as well as they exclude a rotation axis position angle much different than the  $pa_\omega$  derived from visible observations. This confirms the conclusion obtained from the time evolution of the photometric centres (Sect. 2.3), sensitive to both the amplitude and phase of the visibilities.

We compared the observed visibilities to those computed with the model with jet parameters (2), (3) and (4) given in Table 3 (those with  $\theta_\omega = 80^\circ$  and  $pa_\omega = 210^\circ$ ). The lowest  $\chi^2$  (reduced  $\chi^2_{N-n} = 5.1$  for  $N = 150$  data points and  $n = 5$  free parameters) was obtained for the set of parameters (3) with  $\Psi = 18.3^\circ$ ,  $\ell = 20^\circ$  and  $f_{\text{co}} = 35.5\%$ . Simulations with parameters (2) (respectively (4)) show larger (resp. lower) modulations than observed, and  $\chi^2$  val-

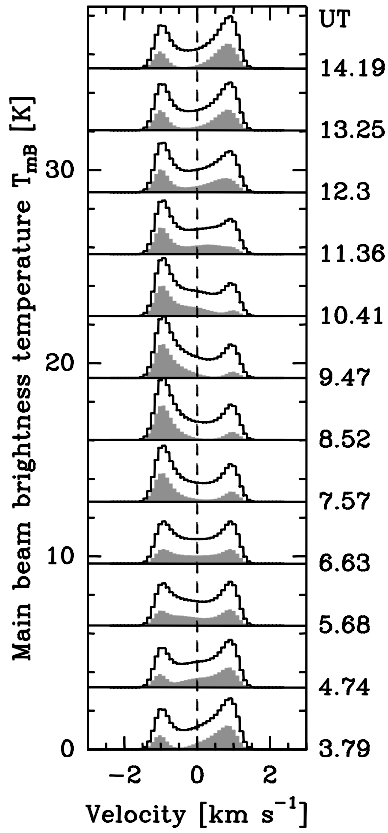


**Fig. 17.** Synthetic CO 230 GHz ON-OFF line profile as a function of UT time on 11 March for parameter set (3) of Table 3 ( $\theta_\omega = 80^\circ$ ,  $pa_\omega = 210^\circ$ ,  $\Psi = 18.3^\circ$ ,  $\ell = 20^\circ$  and  $f_{\text{CO}} = 35.5\%$ ). The total spectrum (jet+isotropic contribution) is shown by thick lines. The grey spectrum shows the contribution of the CO jet.

ues 60% (resp. 22%) larger than with parameters (3). Using jet parameters (3), we also made simulations with  $\theta_\omega = 60$  and  $70^\circ$  and  $pa_\omega = 200, 220$  and  $230^\circ$ . The  $\chi^2$  was minimized for  $pa_\omega = 220^\circ$  ( $\chi^2_{N-n} = 3.8$ ), while  $\theta_\omega$  has no significant influence on the visibilities. However,  $pa_\omega = 210^\circ$  explains better the visibilities of the 3–4 baseline. Figure 21 shows the modelled visibilities with parameters (3) and  $pa_\omega = 210^\circ$ . Looking to the shape of the modulations, there is an overall agreement between model and observations though, admittedly, the agreement is not perfect. A plot of observed versus modelled visibilities shows that the best agreement is for baselines 3–4, 1–5, 1–4, 1–3 and 4–5. The largest discrepancies are for baselines 2–4, 1–2, and 2–5. For most baselines, jet detection (traced by amplitude increase) occurs  $\sim 1$  h earlier in the simulation than in the observations. In contrast, in the velocity shift curves, the simulated jet is late with respect to the observed jet for most baselines. This again shows that our model is too simple to explain satisfactorily the data.

The visibilities obtained when optical depth effects are neglected show the same temporal behaviour (Fig. 22).

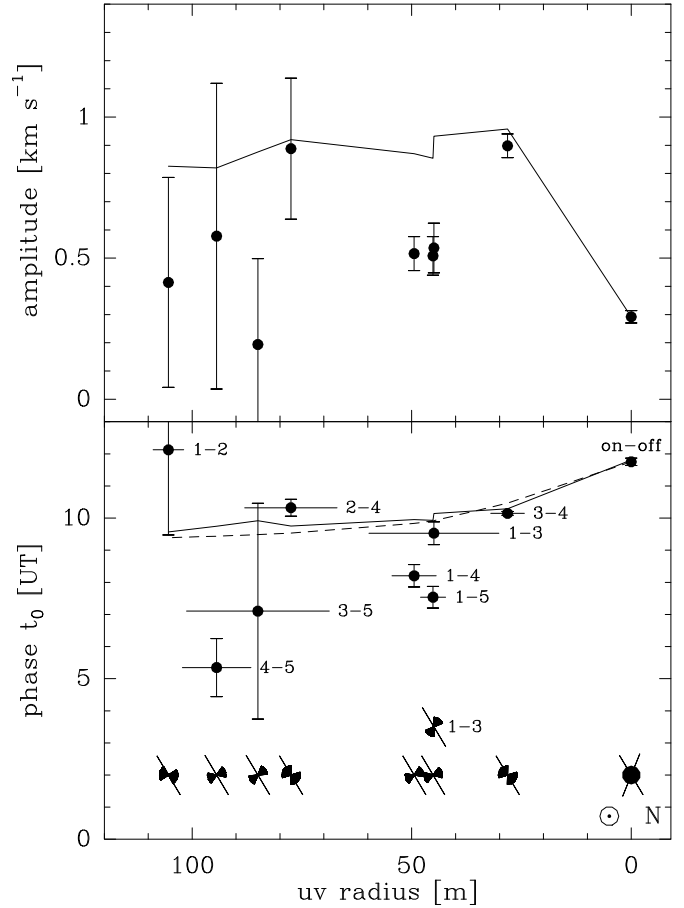


**Fig. 18.** Phase  $t_0$  (bottom) and amplitude  $\mathcal{A}$  (top) of the velocity shift curves as a function of  $uv$ -radius. Dots with error bars are the data. The range of  $uv$  radius spanned by the baselines is shown with horizontal lines in the bottom figure. The plain curve shows model calculations with  $\theta_\omega = 80^\circ$ ,  $pa_\omega = 210^\circ$ ,  $\Psi = 18.3^\circ$ ,  $\ell = 20^\circ$  and  $f_{\text{CO}} = 35.5\%$ . The dotted curve in the bottom figure assumes that the elapsed time between jet detection by baseline at  $uv$ -radius  $\sigma_1$  and jet detection by baseline at  $\sigma_2$  (or in ON-OFF spectrum at  $\sigma_2 = \sigma_1 + 15$  m) is equal to  $(\sigma_2 - \sigma_1)/2v_{\text{exp}}$ , with  $v_{\text{exp}} = 1.05$  km s $^{-1}$ . The reference time is  $t_0$  measured on the ON-OFF velocity shift curve. The orientation of the baselines fringes during the course of the observations is shown at the bottom, together with the spin axis direction in the (RA, Dec) plane: e.g., the field of view of baseline 3–4 has its long dimension (reflecting the primary beam of the antenna) along the spin vector of the comet, and its short dimension (related to the baseline length) perpendicular to it. The Sun direction in the (RA, Dec) plane is also indicated.

However, as expected, modulations are more contrasted in the optically thin case.

The visibilities obtained with jet parameters (3) vary according to  $\tilde{V}(\sigma) \propto \sigma^{-1.24}$ , which is consistent, in first order, with the observed variation ( $\propto \sigma^{-1.18 \pm 0.02}$ ).

#### 4.4. Maps

Simulated maps as a function of time are compared to observed maps in Fig. 23. The shape of the observed CO

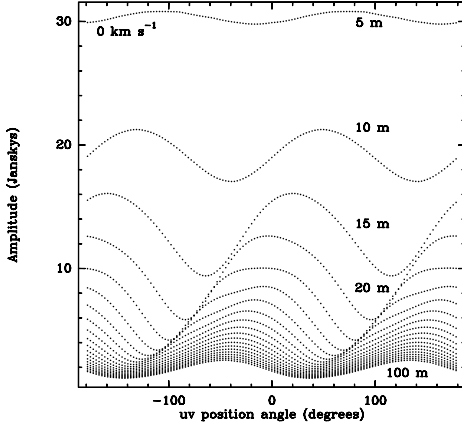


**Fig. 19.** Visibilities of the CO 230 GHz line (central channel) as a function of baseline orientation in the  $uv$  plane and baseline length ( $\sigma$  from 5 to 100 m by step of 5 m) at a given time. The rotation axis ( $P = 11.35$  h) is along the line of sight ( $\theta_\omega = 0^\circ$ ). The jet is equatorial, has an aperture  $\Psi = 30^\circ$ , and its direction at the nucleus surface is at a position angle of  $60^\circ$  in the plane of the sky (i.e.,  $\theta_0 = 30^\circ$ ). Other parameters are  $Q_{\text{CO}} = 1 \times 10^{30} \text{ s}^{-1}$ ,  $f_{\text{CO}} = 1$ , with assumed optically thin conditions.

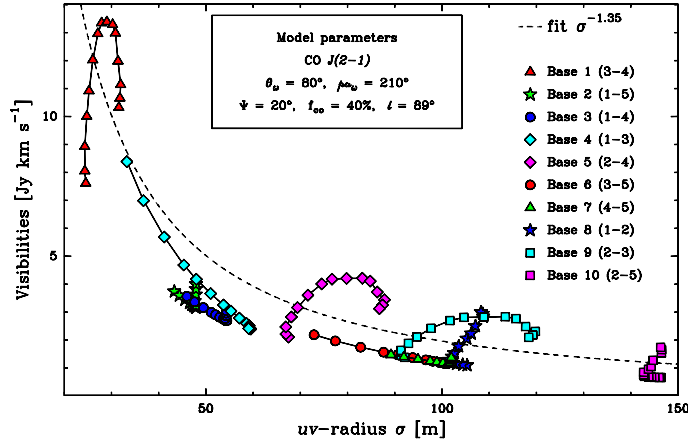


**Fig. 20.** CO 230 GHz modelled visibilities for a high-latitude jet.

coma is relatively well reproduced by the model. Some differences may be due to the presence of other CO coma features, as suggested by noticeable discrepancies at 8h50–9h50 UT. The time evolution of the photometric centre measured on the simulated data (jet parameters (3) with  $pa_\omega = 210^\circ$ ) is shown in Fig. 24. When the position of the photometric centre is referred to the mean photometric centre for the observing period, and is therefore directly comparable to the measurements, there is good agreement in the overall evolution. As could be expected, the relative (modelled–observed) positions generally differ, with discrepancies reaching  $\sim 0.3''$  for 4h30–5h30 and 7h20–8h20 data (maps 1 and 3). However, the good overall agreement confirms a posteriori that the observed time evolution of the CO 230 GHz peak brightness position is related to the CO rotating coma.

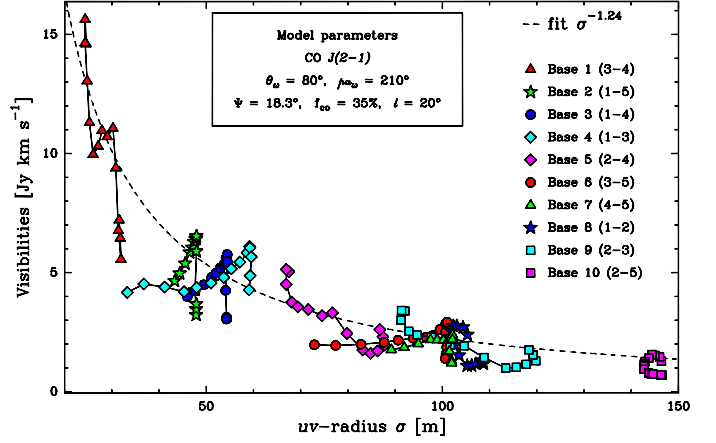


**Fig. 21.** CO 230 GHz modelled visibilities for the jet and rotation axis parameters which reproduce at best the observations (set (3) with  $pa_\omega = 210^\circ$ ).

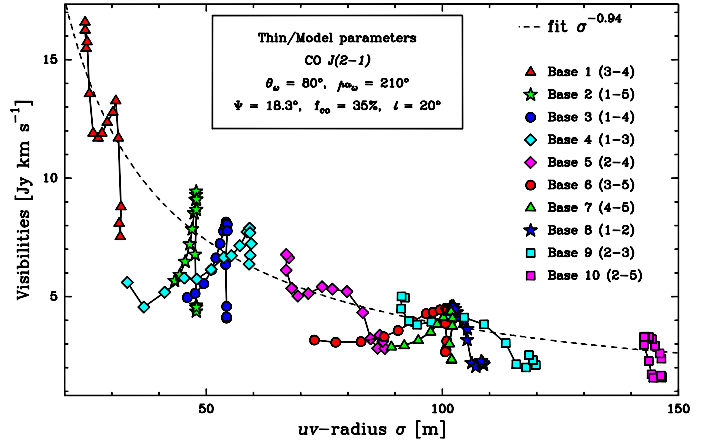


**Fig. 22.** CO 230 GHz modelled visibilities for set (3) with  $pa_\omega = 210^\circ$  assuming an optically thin line.

Synthetic 230 GHz spectral maps directly comparable to the observations (Fig. 6) were computed. Some observed basic features are well reproduced, as the very peaked and strong emission in the blue channels at high velocity and the elongated coma in East-West direction for the blue channels at velocities close to zero. However, the asymmetry of the spatial distribution observed in the red channels is not obtained in the model. As a matter of fact, the model, which parameters were constrained from the large scale ON–OFF observations, predicts that the inner parts of the jet probed during the course of the interferometric observations were most of the time projecting Earthward (i.e., with negative Doppler velocities). The discrepancies between modelled and observed spectral visibilities discussed previously are observed directly on the spectral maps.

#### 4.5. Evidence for a second moving structure

The inability of our one-jet model to reproduce satisfactorily the interferometric data is due to the presence of a second moving CO structure, possibly produced during an outburst.

This moving structure is that seen North-West from the nucleus at positive velocities in the time averaged channel

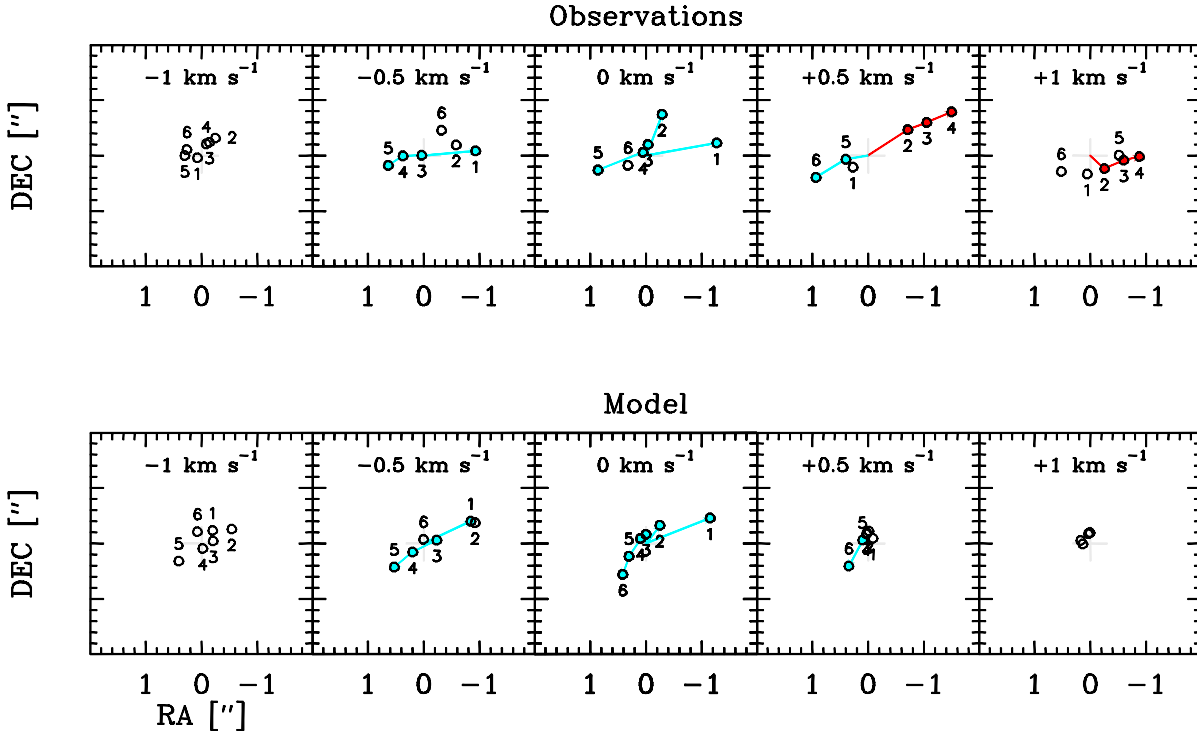


**Fig. 25.** Time evolution of the CO 230 GHz photometric centre for individual velocity channels at  $v = -1.0, -0.5, 0, +0.5, +1.0 \text{ km s}^{-1}$ . The spectral data were smoothed to a spectral resolution of  $0.5 \text{ km s}^{-1}$ . The time intervals labelled 1 to 6 are given in Sect.4.5. Note that they do not correspond to those used for Figs. 23 and 24. The top figure shows the measurements, while the model (set of parameters (3) in Table 3) is shown in the bottom figure. In order to illustrate how the photometric centres are affected by the main jet, we have connected points (coloured in blue) indicative of the motion of the CO main jet. The so-called "red jet" is shown by red symbols.

maps (Fig. 6). This structure, which is moving away from the observer, is oriented along the fringes of baselines 1–4, 1–5, 3–5 and 4–5, i.e., along those for which a strong discrepancy in the time variation of the velocity shift is observed. This structure is essentially detected by these baselines: hence, the velocity shift measured for these baselines is smaller than expected (Fig. 10).

In order to study the time evolution of this structure, the spectral data were smoothed to a spectral resolution of  $0.5 \text{ km s}^{-1}$ , with velocity channels centred at  $-1.0, -0.5, 0, +0.5, +1.0 \text{ km s}^{-1}$  with respect to the comet rest velocity. Five consecutive time intervals (#1, #2, #4, #5, #6) of  $\sim 50 \text{ min}$  to  $1\text{h}30$  long, were considered. The time intervals correspond to characteristic line shapes for the spectrum recorded by baseline 3–4 (Fig. 3): #1 (4h30–5h48 UT) symmetric shape; #2 (5h48–7h07 UT) and #4 (7h07–9h08 UT) asymmetric shape with strong blueshift; #5 (9h08–10h00 UT) symmetric shape; #6 (10h00 UT–11h28) asymmetric shape with high redshift. A sixth period, labelled #3, merging intervals #2 and #4, was also considered.

The  $5 \times 6$  extracted data sets were analysed in the Fourier plane assuming that the brightness distribution is a 2-D Gaussian, with its intensity, width and offset with respect to the line-integrated, time-averaged centre  $C_m$  as free parameters. Figure 25 shows the observed time evolution of the offset ( $RA(t), Dec(t)$ ) for each channel. The same plot is shown using model (3) as input.

For a non-rotating nucleus, the motion of a cloud of gas released during a short time interval from a nuclear source

would be seen by a straight line in the (RA, Dec) quadrant and the velocity channel where its velocity vector projects. For a rotating nucleus, a permanent nuclear source near the equator will produce an expanding jet that will appear successively in the different channels as the nucleus rotates. In the case of comet Hale-Bopp, if the equatorial jet projects North-West in (RA, Dec) at positive velocities channels ( $V_+$ ) at a given time, then it will successively project North-West in negative velocity channels ( $V_-$ ), South-East/ $V_-$ , South-East/ $V_+$ . As shown in Fig. 25, there is a satisfactory agreement between the model and the observations for the channels centred on  $-1.0, -0.5$  and  $0 \text{ km/s}$ . We have tentatively connected the points corresponding to the motion of the CO main jet. At time #1, the jet is Westward in the  $v = 0$  channel, at time #4 it is moving Eastward in the  $v = -0.5 \text{ km s}^{-1}$  channel, at time #5 Eastward in the  $v = 0$  channel, and at time #6 Eastward in the  $v = +0.5 \text{ km s}^{-1}$  channel.

The motion of the red structure is clearly apparent on the channels at  $v = +0.5$  and  $+1 \text{ km s}^{-1}$ . The direction of the motion suggests that it originates from a low latitude region at the nucleus surface. The longitude of this source is estimated to be within  $90\text{--}150^\circ$  westward from the source of the main jet. The weak contribution of the red structure to some baselines can be explained by spatial filtering, implying a compact structure. The CO 230 GHz flux density in channels  $v = +0.5$  and  $+1 \text{ km s}^{-1}$  is four times smaller than in channel  $v = -0.5 \text{ km s}^{-1}$  at the time the CO main



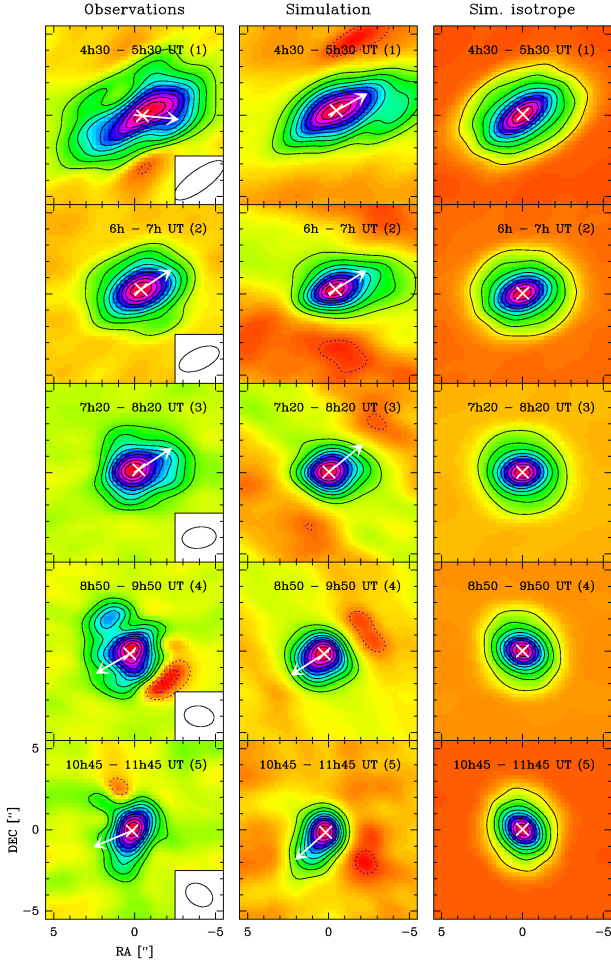


**Fig. 23.** CO 230 GHz Hale-Bopp maps as a function of time. Left column: observations; central column: simulations with the jet and rotation axis parameters which reproduce at best the observations (set (3):  $\theta_\omega = 80^\circ$ ,  $pa_\omega = 210^\circ$ ,  $\Psi = 18.3^\circ$ ,  $\ell = 20^\circ$  and  $f_{\text{co}} = 35.5\%$ ); right column: simulations for an isotropic coma.

jet is contributing. This may explain why the red source does not contribute much to the ON-OFF spectra.

## 5. Discussion

### 5.1. Model assumptions

The observations presented in this paper were interpreted with a simple geometric model of a CO rotating coma. Besides the assumed conical shape of the jet at ejection (see the discussion below), several other simplifying assumptions were made to limit the number of free model parameters. The outflow velocity was fixed and taken to be constant throughout the coma, whereas some acceleration is expected by gas dynamics models (Combi et al., 1999). Day-to-night asymmetries in velocity for the CO background gas were not taken into account either, though they are clearly present. Indeed, the velocity cutoff and width of the blue wing of the CO velocity profiles are 10% higher than the corresponding values for the red wings (Fig. 3), which suggests higher velocities towards the sunlit side of the nucleus given the Earth-comet-Sun geometry. In addition, we assumed that CO molecules inside the jet expand

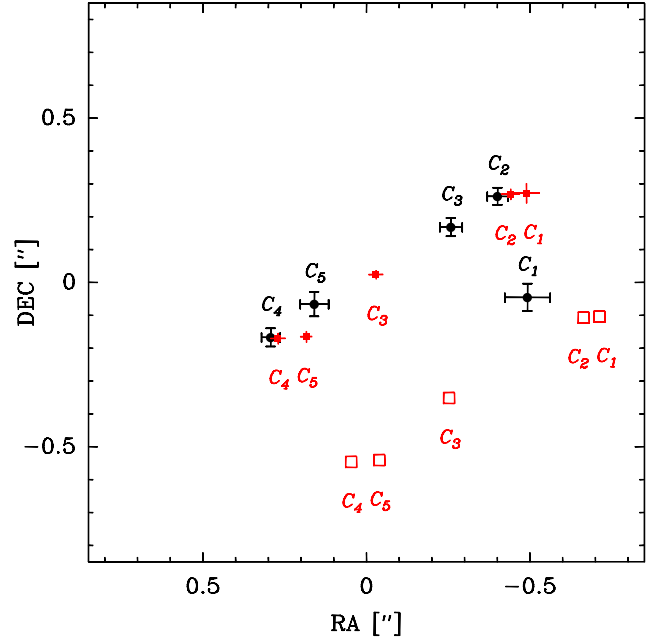


**Fig. 24.** Time evolution of the photometric centre, as determined from fitting in the  $uv$ -plane. Measurements on Hale-Bopp CO 230 GHz observations are shown by black dots with error bars. Those from simulations with jet model (3) ( $pa_\omega = 210^\circ$ ) are plotted with red squares: empty squares show absolute positions; filled squares show photometric centres with respect to the mean photometric center over the period, which can be directly compared to the real data. The accuracy of the photometric centre position measured on the simulated data is also shown.

at the same velocity than those in the background. We believe that including slight variations in the flow velocity field would not change the main conclusions of this paper, though the characteristics of the jet could somewhat differ. For example, including this day-to-night asymmetry in velocity would shift the jet towards lower latitudes. Higher velocities inside the jet would require a proportionally higher jet contribution to the total CO production  $f_{\text{co}}$  to fit the ON-OFF data. We also did not consider possible temperature variations in the coma which have direct effects on CO excitation. A kinetic temperature higher in the jet than in the background gas would have resulted in a higher inferred  $f_{\text{co}}$ . However, a 10 K difference in temperature would change  $f_{\text{co}}$  by less than 10%.

### 5.2. CO jet

Our observations, interpreted with the help of a simple model, suggest the presence of a spiralling "jet" of CO, originating from the nucleus. The rotation of this jet is consistent with the rotation period and axis direction derived from most optical studies. The jet originates from a low-latitude ( $\approx 20^\circ$ ) region of the nucleus, and comprises a significant amount of the total CO production ( $\sim 40\%$ ) in a  $\sim 20$ - $30^\circ$  wide aperture. This is the first evidence of a CO spiralling coma around a comet nucleus. CO ro-vibrational line emissions observed in comet Hale-Bopp from January to May 1997 show strong East/West

asymmetries, with the position of the maximum brightness moving with time from up to  $\sim 2''$  West to  $\sim 2''$  East of the continuum peak (DiSanti et al., 2001; Brooke et al., 2003). This is likely caused by the rotating CO structure observed in the radio (Brooke et al., 2003) and shows that this CO structure was not a transient phenomenon related to some outburst.

Our model, which includes a single jet, appears to be too simple to interpret all observation characteristics. Other "jets" are present, in particular another moving structure has been identified at positive velocities in the interferometric data. Its full characterization is difficult from our data and beyond the scope of this paper. The CO main jet is certainly more complex than a simple conical spiralling structure. Gas structures created by inhomogeneities in gas production at the nucleus surface will unescapably be modified during their outflow by the surrounding collisional environment (the collisional sphere in Hale-bopp coma exceeded  $10^5$  km near perihelion, Combi et al., 1999).

Gas dynamics models investigating the behavior of expanding dusty gas jets have been developed (see the review of Crifo et al., 2005). One or several active sources releasing water were considered, the rest of the nucleus being assumed to be weakly active. They show that, due to lateral expansion driven by pressure gradients, jets broaden with increasing distance to nucleus and interact with each other, to become eventually almost indiscernible in the outer coma. In addition, if there is solar modulation of the surface gas flux, the jet morphology will change its appearance as the nucleus rotates. So far, these calculations may not be relevant to the CO jet seen in comet Hale-Bopp. First of all, it is very likely that CO diffuses from subsurface layers. Our observations suggest that, in first order, there is no significant day-to-night asymmetry in the amount of CO gas released by the active source. Second, if the active source responsible for the CO jet does not produce similar strong enhancement in water production, pressure smoothing will not be acting much and jet broadening may rather result from molecular diffusion. In this case, it is possible that a nearly invariant CO density pattern co-rotates with the nucleus and remains relatively well preserved at large scales in the coma. However, it can be anticipated that the jet development will be still influenced by the surrounding environment.

A good illustration is the following. Rodionov & Crifo (2005) performed time-dependent 3-D gas dynamics calculations simulating rotationally-induced gas coma structures. They used an arbitrarily Halley-like aspherical nucleus, scaled to Hale-Bopp nucleus size and homogeneous in composition. CO was assumed to diffuse uniformly from below the surface, while H<sub>2</sub>O sublimates according to solar illumination. The computed CO coma is asymmetric. The model produces faint H<sub>2</sub>O and CO spiralling structures resulting from weak shocks induced by the surface topography. In other words, the CO outflow is largely influenced by the general and detailed properties of the flow. The analysis of the CO Plateau de Bure observations using time-dependent (multi-fluid) gas dynamics calculations was performed by Boissier et al. (2005, 2009). They show that the observed time variations cannot be explained by the above mentioned shock structures and is due to a strong inhomogeneity in CO production from the nucleus surface or sub-surface. It is possible to hypothesize lengthly about the meaning of this CO overproduction. It can traduce in-

homogeneities in CO content inside the nucleus but also local variations in mantle thickness, or in some properties of the nucleus material (e.g., dust/ice matrix structure, thermal conductivity). We leave this discussion to experts and encourage them to perform numerical simulations (see the review of Prrialnik et al., 2005).

### 5.3. Comparison with other studies

Two questions arise:

1) Is the CO jet we observed related (correlated) to jets observed for other molecules?

2) Is the CO jet we observed related (correlated) to observed dust jets?

In their interferometric observations of several molecular species (HCN, HNC, DCN, HDO) with the OVRO array, Blake et al. (1999) observed that the molecular emissions peak at positions offset by a few arcsec from the continuum emission of the comet, and attributed these offsets to molecular jets. We do not observe such large offsets for CO when averaging the data over 70% of the rotation period. However, offsets reaching  $1-1.5''$  were observed for other molecules observed at the PdBI, interpreted to be the gaseous signatures of the high latitude dust jet observed in the visible (Boissier et al., 2007). The strong CO jet has no strong H<sub>2</sub>S, CS, SO and HCN counterparts though weak rotational modulations in the line shapes of their radio emission are observed for some of them (Boissier et al., 2007).

Lederer & Campins (2002) and Lederer et al. (2009) observed spiralling jets of OH, CN and C<sub>2</sub>. Several (up to five) active areas were necessary to reproduce their observations from their Monte Carlo simulation. The strongest jets are coming from low-latitude regions ( $-22^\circ$  to  $+20^\circ$ ). One of them could thus be associated with our CO jet. One low-latitude southern area is responsible for one-half of the OH coming from jet-source, but has a large opening angle ( $120^\circ$ ). So it is likely not related to the CO jet. Spatial profiles of H<sub>2</sub>O obtained from long-slit observations of infrared water lines only show small East-West asymmetries (Dello Russo et al., 2000). In summary, there is no strong evidence for a strong H<sub>2</sub>O jet associated to the CO jet.

Woodney et al. (2002) mapped HCN in comet Hale-Bopp with the BIMA array. Their observations, which spanned over several days, were binned and averaged according to the phase of the comet rotation, in order to avoid smearing due to rotation. They found a jet morphology, possibly correlated with CN imaged in the visible. However, there is apparently no correlation of HCN with dust jets. The presence of a high-latitude HCN jet is however suggested from the PdBI data (Boissier et al., 2007).

Dust jets also appear to be uncorrelated with our CO jet. Indeed, from visible imaging at the time of the PdBI observations, Jorda et al. (1999) observed a high latitude ( $64^\circ$ ) dust jet. In the analysis of Vasundhara & Chakraborty (1999), strong dust jets are present from latitudes  $+65^\circ$  and  $-65^\circ$ , in addition to weaker jets from low latitudes (see also Schleicher et al., 2004). In February–May 1997, the high-latitude northern jet produced repetitive sunward shells instead of a full spiral (Fig. 26), indicating that the source of this dust jet shut off during night time in contrast to the CO jet.

In addition to the CO main jet, we have identified a second moving structure in red channels that we believe originates from a low latitude source. Interestingly, on 12.14

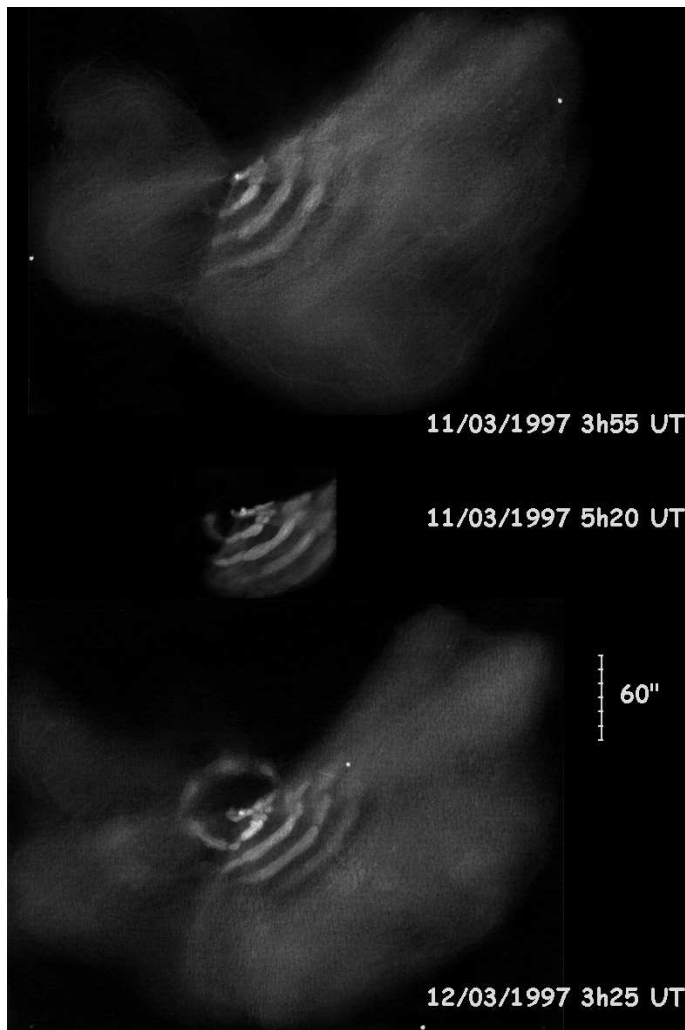


**Fig. 26.** Drawings of the inner coma of comet Hale-Bopp on 11 and 12 March, 1997 (N. Biver, 25.6 cm Newtonian telescope).

March 1997 UT the dust coma presented a well defined shell at  $\sim 40''$  in a direction opposite to the repetitive sunward shells produced by the high-latitude sources (Fig. 26). This shell was not present on 11.16 March, nor on 14.80 March, and can be attributed to an outburst initiated on 11.20 March UT, i.e., at the time when the red structure began its expansion. Possibly, the red structure is related to this outburst.

#### 5.4. Plans for further studies

ON-OFF and interferometric data were obtained at the Plateau de Bure interferometer for HCN, HNC, CS, H<sub>2</sub>S, SO, H<sub>2</sub>CO and CH<sub>3</sub>OH (Wink et al., 1999; Boissier et al., 2007). Some lines (e.g., lines of HCN and CS) do show rotation-induced variations in their velocity shifts. The analysis of the Plateau de Bure observations is continuing and will be presented in forthcoming papers.

The present study showed that radio observations can provide valuable information on the distribution of parent molecules in inner cometary atmospheres and its temporal evolution. In contrast with standard imaging techniques, radio observations are sensitive to radial velocities, i.e. they

are sensitive to the gas distribution along the line of sight, whereas the other techniques are rather sensitive to the distribution on the plane of the sky. They also probe different gas species. Radio observations and other techniques are therefore complementary.

Radio interferometric imaging is a powerful tool for astrometry. Our observations show that, in addition, rotating comas can be detected from the motion of the centroid of molecular maps. This opens new perspectives because possibly useful constraints on the rotation properties of cometary nuclei will be obtained from such measurements.

The analysis of our interferometric data was hampered by the limited instantaneous *uv*-coverage of the Plateau de Bure interferometer. The Atacama Large Millimeter and submillimeter Array (ALMA), with its 50 antennas, will be able to obtain images of molecular and continuum emissions with a short sampling time, high sensitivity and high angular resolution. It will provide a 3-D dynamical picture of inner cometary gaseous atmospheres, simultaneous images of the dust coma, and spatial information on the gas temperature (Biver, 2005; Bockelée-Morvan, 2008). Important breakthroughs concerning nucleus and coma processes can be expected.

*Acknowledgements.* This paper is dedicated to Jörn Wink, who performed these marvellous observations and helped us in their analysis despite his terrible illness. We gratefully thank the IRAM staff, for help in the observations, and P. Rocher (IMCCE, Observatoire de Paris) for providing us with detailed ephemeris of comet Hale-Bopp. We thank Jean-François Crifo for enlightening discussions about coma hydrodynamics. Many thanks also to Anne Dutrey for constant support, and to Laurent Jorda, for helpful exchanges about comet Hale-Bopp rotation. IRAM is an international institute co-funded by the CNRS, France, the Max-Planck-Gesellschaft, Germany, and the Instituto Geográfico Nacional, Spain. This work has been supported by the Programme national de planétologie of Institut national des sciences de l'univers.

## References

- Altenhoff, W. J., Bieging, J.H., Butler, B., et al. 1999, *A&A*, 348, 1020
- Biver, N. 2005, *The Dusty and Molecular Universe. A prelude to Herschel and ALMA*, ESA SP-577, 151
- Biver, N., Bockelée-Morvan, D., Colom, P., et al. 1997, *Science*, 275, 1915
- Biver, N., Winnberg, A., Bockelée-Morvan, D., et al. 1998, *BAAS*, 30, 5519
- Biver, N., Bockelée-Morvan, D., Colom, P., et al. 1999a, *Earth, Moon & Planets*, 78, 5
- Biver, N., Bockelée-Morvan, D., Crovisier, J., et al. 1999b, *AJ*, 118, 1850
- Blake, G.A., Qi, C., Hogerheijde, M.R., Gurwell, M.A., & Muhleman, D.O. 1999, *Nature*, 398, 213
- Bockelée-Morvan, D., Lis, D. C., Wink, J. E., et al. 2000, *A&A*, 353, 1101
- Bockelée-Morvan, D. 2008, *Astrophysics and Space Science* 313, 183
- Bockelée-Morvan, D., Crovisier, J., Mumma, M.J., & Weaver, H.A. 2004, in *Comets II*, ed. M.C. Festou, H.U. Keller, & H.A. Weaver (The University of Arizona Press, Tucson), 391
- Bockelée-Morvan, D., Boissier, J., Crovisier, J., Henry, F., & Weaver, H.A., 2005, *BAAS*, 37, 633
- Bockelée-Morvan, D., & Boissier, 2009, *A&A*, in preparation
- Boissier, J., Bockelée-Morvan, D., Crifo, J., & Rodionov, R. 2005, *Asteroids, Comets, Meteors*, Buzios, August 7-12, 2005, book of abstract.
- Boissier, J., Bockelée-Morvan, D., Rodionov, R., & Crifo, J. 2009, *A&A*, in preparation
- Boissier, J., Bockelée-Morvan, D., Biver, N., et al. 2007, *A&A*, 475, 1131
- Brooke, T.Y., Weaver, H.A., Chin, G. et al. 2003, *Icarus*, 166, 167
- Capria, M.T., Coradini, A., De Sanctis, M.C., & Orosei, R. 2000, *A&A*, 357, 359

- Capria, M.T., Coradini, A., & De Sanctis, M.C. 2002, *Earth, Moon & Planets*, 90, 217
- Colom, P., Grard, E., Crovisier, J., et al. 1999, *Earth, Moon, & Planets*, 78, 37
- Combi, M.R., Kabin, K., DeZeeuw, D.L., Gombosi, T.I., & Powell, K.G. 1999, *Earth, Moon & Planets*, 79, 275
- Crifo, J.F., Fulle, M., Kömle, N.I., & Szego, K. 2005, in *Comets II*, ed. M.C. Festou, H.U. Keller, & H.A. Weaver (The University of Arizona Press, Tucson), 471
- Crovisier, J. 1987, *A&AS*, 68, 223
- Crovisier, J., & Le Bourlot, J. 1983, *A&A*, 123, 61
- Crovisier, J., Biver, N., Bockelée-Morvan, D., et al. 1995, *Icarus*, 115, 213
- Crovisier, J., Bockelée-Morvan, D., Biver, et al. 2004a, *A&A*, 418, L35
- Crovisier, J., Bockelée-Morvan, D., Colom, P. et al. 2004b, *A&A*, 418, 1141
- Dello Russo, N., Mumma, M.J., DiSanti, M., et al. 2000, *Icarus* 143, 324
- Despois, D. 1999, *Earth, Moon & Planets*, 79, 103
- DiSanti, M.A., Mumma, M.J., Dello Russo, N., et al. 1999, *Nature*, 399, 662
- DiSanti, M., Mumma, M., Dello Russo, N., & Magee-Sauer, K. 2001, *Icarus*, 153, 361
- Eberhardt, P., Krankowsky, D., Schulte, W., et al. 1987, *A&A*, 187, 481
- Enzian, A., Cabot, H., & Klinger, J. 1998, *Planetary Space Science*, 46, 851
- Farnham, T.L., Schleicher, D.G., Williams, W.R., & Smith, B.R. 1999, *BAAS*, 31, 3001
- Henry, F. 2003, *La comète Hale-Bopp à l'interféromètre du Plateau de Bure: étude de la distribution du monoxyde de carbone*, PhD Thesis, University of Paris 6
- Henry, F., Bockelée-Morvan, D., Crovisier, J., & Wink, J. 2002, *Earth, Moon & Planets*, 90, 57
- Huebner, W., Keady, J., & Lyon, S. 1992, *Ap&SS*, 195, 7
- Irvine, W.M., Schloerb, F.P., Crovisier, J., Fegley, B., Jr., & Mumma, M.J. 2000, in *Protostars and Planets IV*, ed. V. Mannings, A.P. Boss, & S.S. Russel (The University of Arizona Press, Tucson), 1159
- Jorda, L., Rembor, K., Lecacheux, J., et al. 1999, *Earth, Moon & Planets*, 77, 167
- Lederer, S.M., & Campins, H. 2002, *Earth Moon & Planets*, 90, 381
- Lederer, S.M., Campins, H., & Osip, D.J. 2009, *Icarus*, in press
- Licandro, J., Bellot Rubio, L.R., Boehnhardt, H., et al. 1998, *ApJ*, 501, L221
- Licandro, J., Bellot Rubio, L.R., Casas, R., et al. 1999, *Earth Moon & Planets*, 77, 199
- Metchev S., & Luu J., In 1<sup>st</sup> International Conference on Hale-Bopp, Tenerife, Spain, February 2-5, 1998
- Mouis, O., Gautier, D., Bockelée-Morvan, D., Robert, F., & Dubrulle, B. 2000, *Icarus*, 148, 513
- Ortiz, J.L., & Rodríguez, E. 1999, *Earth, Moon & Planets*, 77, 207
- Prialnik, D., Benkhoff, J., & Podolak, M. 2005, in *Comets II*, ed. M.C. Festou, H.U. Keller, & H.A. Weaver (The University of Arizona Press, Tucson), 359
- Rodionov, A.V., & Crifo, J.F. 2005, *Adv. Space Res.*, in press
- Sarmecanic, J.R., Osip, D.J., Lederer, S.M., Fomenkova, M.N., & Jones, B. 1997, *BAAS*, 29, 3207
- Schleicher, D.G., Farnham, T.L., & Hawley, W. 2004, *BAAS*, 36, 1126
- Sekanina, Z., & Boehnhardt, H. 1999, *Earth, Moon & Planets*, 78, 313
- Sekanina, Z., Boehnhardt, H., Womack, M., et al. 1997, *IAU Circ. No* 6542
- Senay, M., & Jewitt, D. 1994, *Nature* 371, 229
- Snyder, L.E., Veal, J.M., Woodney, L.M., et al. 2001, *AJ*, 121, 1147
- Thompson, A., Moran, J., & Swenson, G. 1991, *Interferometry and Synthesis in Radio Astronomy*, Krieger Publishing Company (eds.)
- Vasundhara, R., & Chakraborty, P. 1999, *Icarus*, 140, 221
- Veal, J.M., Snyder, L.E., Wright, M., et al. 2000, *AJ*, 119, 1498
- Wink, J., Bockelée-Morvan, D., Despois, D., et al. 1999, *Earth, Moon & Planets*, 78, 63
- Woodney, L.M., A'Hearn, M.F., Schleicher, D.G., et al. 2002, *Icarus*, 157, 193
- Wright, M.C.H., de Pater, I., Forster, J.R., et al. 1998, *AJ*, 116, 3018